THE UNIVERSITY OF ALBERTA

DESIGN AND APPLICATION OF LOW ENERGY ION BEAM OPTICS

BY

KOK-KEN FOO

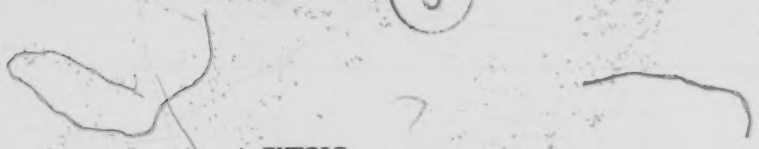

A THESIS

SUBMITTED TO THE FACULTY OF GRADUATE STUDIES AND RESEARCH IN PARTIAL FULFILLMENT OF THE REQUIREMENTS FOR THE DEGREE OF

MASTER OF SCIENCE

DEPARTMENT OF ELECTRICAL ENGINEERING

EDMONTON, ALBERTA

SPRING 1991

National Library of Canada
Bibliothèque nationale du Canada

Canadian Theses Service
Service des thèses canadiennes

Ottawa, Canada
K1A 0N4

The author has granted an irrevocable non-exclusive licence allowing the National Library of Canada to reproduce, loan, distribute or sell copies of his/her thesis by any means and in any form or format, making this thesis available to interested persons.

L'auteur a accordé une licence irrévocable et non exclusive permettant à la Bibliothèque nationale du Canada de reproduire, prêter, distribuer ou vendre des copies de sa thèse de quelque manière et sous quelque forme que ce soit pour mettre des exemplaires de cette thèse à la disposition des personnes intéressées.

The author retains ownership of the copyright in his/her thesis. Neither the thesis nor substantial extracts from it may be printed or otherwise reproduced without his/her permission.

L'auteur conserve la propriété du droit d'auteur qui protège sa thèse. Ni la thèse ni des extraits substantiels de celle-ci ne doivent être imprimés ou autrement reproduits sans son autorisation.

ISBN 0-315-66691-9

Canada

THE UNIVERSITY OF ALBERTA

RELEASE FORM

NAME OF AUTHOR: KOK-KEN FOO

TITLE OF THESIS: **DESIGN AND APPLICATION OF LOW ENERGY ION BEAM OPTICS**

DEGREE: MASTER OF SCIENCE

YEAR THIS DEGREE GRANTED: SPRING 1991

PERMISSION IS HEREBY GRANTED TO THE UNIVERSITY OF ALBERTA LIBRARY TO REPRODUCE SINGLE COPIES OF THIS THESIS AND TO LEND OR SELL SUCH COPIES FOR PRIVATE, SCHOLARLY OR SCIENTIFIC RESEARCH PURPOSES ONLY.

THE AUTHOR RESERVES OTHER PUBLICATION RIGHTS, AND NEITHER THE THESIS NOR EXTENSIVE EXTRACTS FROM IT MAY BE PRINTED OR OTHERWISE REPRODUCED WITHOUT THE AUTHOR'S WRITTEN PERMISSION.

SIGNED _____

PERMANENT ADDRESS:

12231-156 AVE.,

EDMONTON, ALBERTA,

T5X 2X3

DATED 19th Dec 1990

THE UNIVERSITY OF ALBERTA

FACULTY OF GRADUATE STUDIES AND RESEARCH

The undersigned certify that they have read, and recommend to the Faculty of Graduate Studies and Research, for acceptance, a thesis entitled "Design and Application of Low Energy Ion Beam Optics" submitted by KOK-KEN FOO in partial fulfillment of the requirements for the degree of MASTER OF SCIENCE.

Dr. RPW Lawson (Co-Supervisor, U of Alberta)

Dr. WM Lau (Co-Supervisor, U of Western Ontario)

Dr. MJ Brett

Dr. S Sheinin (External Examiner)

Date 18 Dec 1990

Dedication

To my parents

and Jasmine

FOR THEIR SUPPORT.

Abstract

A compact mass-resolved low energy ion beam system has been constructed at the University of Western Ontario. Ions are extracted from a Colutron source, focused by an Einzel lens, mass-selected by a Wien filter, refocused by a second Einzel lens into an UHV target chamber, and finally decelerated with a five-electrode lens. The performance of the deceleration lens was assisted by a computer simulation program (CHDEN) with space-charge effect included. The performance of the deceleration lens was characterized by a quadrupole mass spectrometer and a beam profile monitor. Ar^+ can be decelerated to 10eV with an energy spread of ±0.5eV. The diameter of a 50eV In^+ beam at FWHM, measured by the beam profile monitor, was about 1.9mm. The beam scanning system, built to achieve more uniform solid-ion interaction, was tested by depositing a uniform film of indium. The uniformity of the indium film was verified by XPS. Finally, the addition of a mass-switching unit has enabled beam switching between two distinctly separate ions species: In^+ and N_2^+ and has produced interesting results in the deposition of indium nitride.

Acknowledgements

I wish to thank my supervisors, Dr. Leo Lau and Dr. Ronald Lawson, for their assistance and encouragement during the course of this work and thoughout the writing of this thesis.

This work was funded by the Natural Science and Engineering Research Council of Canada and the University of Alberta. I wish to express my gratitude to these bodies.

I also wish like to express my appreciation to the following people:

Dr. N.S. McIntyre at Surface Science Western, for the usage of analytical equipment.

Dr. I. Bello, Dr. S. Sant, and Dr. X. Feng at Surface Science Western, for their collaboration in constructing the UHV equipment.

Mr. G. Good of Surface Science Western, for his assistance with the electronics and maintenance of equipment.

Mr. H. Chen of Physics Department at U of Western Ontario, for his assistance with and lending of electronic equipment.

Mr. W.H. Chang, at Surface Science Western for his assistance with XPS.

Dr. S. Ramanmurphy, at Surface Science Western for his assistance with electrochemical cleaning.

Mr. R. Schmaus, for his assistance with the electronics and ion beam components.

Table of Contents

	Page
PART I Introduction	1
Chapter 1 Background	2
1.1 Ion beam systems	2
1.1.1. General survey	2
1.1.2. Advantages	3
1.1.3. Disadvantages	5
1.1.4. Goals	6
1.2 Low energy ion beam deposition system	7
1.2.1. Ion sources	9
1.2.2. Beam focusing system	14
1.2.3. The Wien (velocity) filter	14
1.2.4. UHV generation	15
1.2.5. Vacuum gauges	17
1.2.6. The VG quadrupole spectrometer	17
PART II Description of the ion optics constructed in this study - the deceleration lens, the beam scanning and profiling unit, and mass-switching unit	24
Chapter 2 The deceleration system	25
2.1 Requirements for the deceleration system	25
2.2 Theory	26
2.2.1. Analytical methods	26
2.2.2. Numerical methods	28
2.3 Design of the deceleration lens	29

2.4 Construction 37

2.5 Evaluation of the deceleration lens 39

Chapter 3 Rastering and profiling system 44

3.1 Specification 46

3.2 Electronics design 50

3.3 Evaluation 52

Chapter 4 Switching of sequential beams 55

4.1 Ion source for sequential beams 55

4.2 Construction 56

4.3 Evaluation 58

PART III System Applications 60

Chapter 5 Thin film deposition 61

5.1 Background 61

5.1.1. In and InN deposition 61

5.1.2. XPS analysis 62

5.1.2.1. Theory 62

5.1.2.2. Instrumentation 64

5.2 Results and Discussions 69

5.2.1 In films 69

5.2.2 Preliminary results on InN deposition 75

PART IV Conclusions 79

Chapter 6 Conclusions 80

PART V References 81

PART VI VITA 90

List of Tables

Page

Table 2.1. Sets of deceleration voltages used to determine the optimized lengths. 35

Table 5.1. Relationship between pass energy and analyzer resolution. 67

Figure Captions

	Page
Figure 1.1. IBD publication yield.	4
Figure 1.2. The energy and mass resolved low energy ion beam system at the University of Western Ontario.	8
Figure 1.3. Potential and field diagram of the hot cathode electron impact ion source.	11
Figure 1.4. Outgassing behavior of a metal ion source (hot cathode electron impact type) as a function of pressure and filament current.	13
Figure 1.5. Configuration of a Wien (ExB) filter.	16
Figure 1.6. Optics assembly of the VG SPX-300 QMS.	19
Figure 1.7. Potential in the quadrupole from external supplies.	19
Figure 1.8. Solutions for Mathieu equations.	22
Figure 1 9. Mass scan through the stable region for both x and y directions near the origin.	22
Figure 2.1. The ion optics control.	30
Figure 2.2. Ion paths and potential gradients to illustrate: (a) HLH focusing mode; and (b) LHL focusing mode.	33
Figure 2.2. (c) Beam diameter of electrodes with equal and optimized lengths.	34
Figure 2.3. Ion paths and potential gradients: (a) five-electrode focusing mode and (b) Single-step deceleration.	36
Figure 2.4. Decelerattion lens and target configuration.	38
Figure 2.5. Ar^+ beam current density at the target as a function of beam enefgy for the two deceleration lens configurations.	41

Figure 2.6. Ar^+ beam current density at the target for various optimum lens voltage configurations. 42

Figure 2.7. Ar^+ beam profile at 100 eV beam energy. 43

Figure 3.1. Deposition time and thickness (monolayers) as a function of different beam diameters. 45

Figure 3.2. Electrical block diagram of the beam profiling and rastering system. 47

Figure 3.3. Physical layout of a beam deflection system. 49

Figure 3.4. Schematic diagrams of: (a) High Voltage controller; and (b) optical isolated High Voltage amplifier. 51

Figure 3.5. Beam profiles of: (a) N_2^+; and (b) In^+ at 50 eV. 53

Figure 3.6. Deposition time and thickness (monolayers) as a function of different rastering areas. 54

Figure 4.1. Flowchart for the beam switching control. 57

Figure 4.2. Mass spectrum of: (a) In^+; and (b) N_2^+ during sequential ion beams switching. 59

Figure 4.3. Energy spectrum of In^+ at 100 eV. 59

Figure 5.1. Graphical representation of compiled inelastic electron mean free path (IMFP) for elements in monolayers (λ_m) as a function of electron energy. 65

Figure 5.2. (a) Schematic representation of X-ray photoelectron emission process; (b) Instrumentation setup for SSX-100 'small spot' ESCA. 66

Figure 5.3. XPS spectral outputs of In deposition at different spot sizes and analyzer resolution: (a) survey scan, 300 μm, 70

1.5 eV; (b) In window, 300 μm, 0.25 eV; and (c) valence-band, 300 μm, 1.0 eV.

Figure 5.4. In^+ beam profile at 50 eV with current contours. 73

Figure 5.5. Thickness of indium in: (a) x-direction; and (b) y-direction of actual deposition. Thickness of indium in: (c) x-direction; and (d) y-direction from simulation. 74

Figure 5.6. XPS spectra of In_xN_y at: (a) In (3d 5/2); and (b) valence-band edge. 77

Figure 5.7. XPS spectrum of silicon nitride. 78

Part I Introduction

Chapter 1. Background

1.1 Ion Beam Systems

1.1.1 General Survey

The increasing demand for thin films in recent years has led to growing research in the technology of film deposition. New growth methods are being studied to improve film properties such as stoichiometry, composition and crystalline structure. In general, the film growth mechanism depends on many factors such as substrate temperature, surface environment, and substrate material. The deposition method, which governs the state of the incoming (depositing) species, is also an important parameter in the quality of the growing film.

The present thesis examines one of the many film growth techniques - low energy ion beam deposition (LEIBD). LEIBD is a subset of ion beam deposition (IBD) technology which also includes ion beam sputtering deposition and ion cluster beam deposition. The ion beam sputtering deposition method is a process in which an ion beam (eg. Ar^+) is directed to a solid source. The materials ejecting from the source are intercepted by a substrate and eventually condense on it[1,2]. The energy of the sputtered particles is usually in the range of a few tens of eV. Ion cluster beam deposition is a process in which atoms in a supersaturated vapor, produced by adiabatic expansion through a small nozzle, are partially ionized by electron impact ionization[3,4]. The partially ionized vapor is

transported by an electrostatic field to the target. Since the energy of a few charged atoms is shared by all the deposited atoms, the average energy per atom can be set to a few eV.

Low energy ion beam deposition (LEIBD) is a technique in which ions are extracted from an ion source, accelerated, mass-filtered and decelerated before reaching the target. The range of the impact energy for the low energy ion, as we define it, is from 0 to 200 eV. This technique has the greatest flexibility in controlling the purity and energy of the depositing species. Therefore, LEIBD was chosen for the University of Western Ontario system as the preferred technique for studying the ion-solid interactions during the film growth process.

1.1.2 Advantages

Because of the inherent advantages of depositing low energy ions directly to a substrate, LEIBD has become increasingly important in the past few years. The growing interest in LEIBD is clearly shown by the number of publications in Fig. 1.1. One of the distinct advantages that LEIBD has is the mass-resolved capability. Unwanted ion species are always filtered out to ensure high purity for the deposited film. In fact, isotopically pure films have been deposited with this technique[8]. Since the growth process is carried out in a clean ultra high vacuum environment, purity of the film is further ensured. Because of the mass-selective ability, sequential ion beam deposition has been made possible by several researchers[5-7].

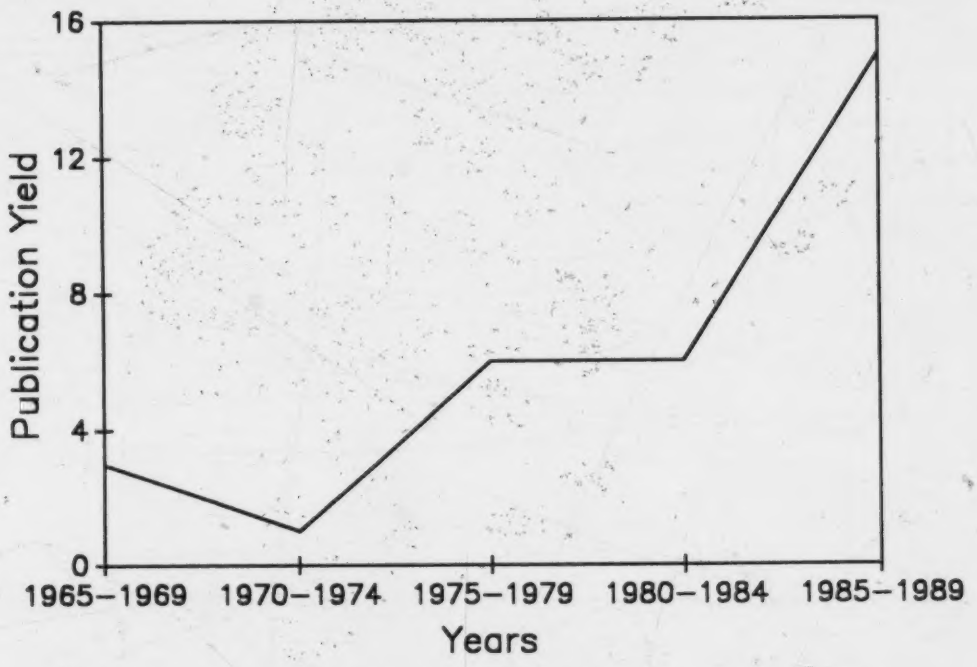

Figure 1.1 IBD Publication Yield.

Sequential ion beam deposition provides a unique opportunity in tailoring film composition and film structure.

The energy-selecting ability of LEIBD maximizes adhesion and minimizes sputtering[8-11]. By altering the ion impact energies, the sticking coefficient of the depositing ions can be made to approach unity. In addition, the ion impact energy may also enhance surface migration and thereby promote epitaxial growth. Epitaxial growth of Si at temperature as low as 100 °C has been shown to be possible with impact energy at 50 eV[12]. Epitaxial growth of Ge on Si is also possible at low temperature (≈ 300 °C)[13,14]. Room temperature oxidation has been demonstrated with a silicon vapor and an O_2^+ beam to bypass the chemisorption, physisorption and diffusion processes which require a higher temperature in order to proceed[15].

1.1.3 Disadvantages

The main disadvantage for low energy ion beam facilities is that they are all costly. For example, even the relatively modest low energy ion beam system (LEIBS) at the University of Western Ontario costs approximately CDN. $300,000. Such a system is costly to maintain and difficult to operate unless it is automated[16].

When the ions are decelerated to the low energy regime (0 - 200 eV), the ion current density decreases due to space-charge effect. The space-charge repulsion causes the beam diameter to increase which in turn reduces the current intensity drastically.

Therefore, it is critical to design an efficient deceleration system to minimize the current loss due to space-charge repulsion[5,6,17,18].

In addition, the ion current density as well as total current may also be reduced by gas phase neutralization during beam transportation[11]. A limited current density may lead to an unacceptably slow growth rate. Furthermore, film purity may become a problem if the arrival rate of residual gases in the deposition chamber is comparable to the ion arrival rate. However, the ion arrival rate can be improved by incorporating a high current output source which results in the increase of film growth rate[19]. Finally, the detailed growth mechanism of LEIBD is not very well understood although an excellent growth model has been proposed[6].

1.1.4 Goals

The main goals of this thesis are three-fold: (1) construction of a deceleration lens to facilitate the generation of low energy ion beams with a current density greater than 1 $\mu A/cm^2$; (2) construction of a beam scanning and profiling unit to provide an uniform beam bombardment area and determine the size of the ion beam and (3) construction of a beam mass-switching unit for the deposition of binary compounds.

The deceleration lens will be simulated by an ion path simulation program CHDEN. Performances of the final design will be verified experimentally. The current density delivered by the

deceleration lens will be measured by a Faraday cup. Focusing ability of the lens can be determined by moving the Faraday cup manually or using the computerized beam profiling unit.

The control circuits for the beam scanning, profiling and mass-switching unit will be constructed in a single unit although the ion optics involved are different. Operations of these units will be tested and verified independently even though they will be merged to assist in the later deposition experiment. By depositing a uniform thin film on a substrate, the beam scanning operation will be verified. Finally, a quadrupole mass spectrometer will be used to characterize the depositing ion species during mass-switching operation.

1.2 The Low Energy Ion Beam System at UWO

The low energy ion beam system (LEIBS) constructed at the University of Western Ontario, a slight modification of the Colutron G-2 Ion Gun model[20], is shown in Fig. 1.2. The ion generating and transporting system consist of: a) Colutron model-100 ion source; b) two Colutron model-200 Einzel lenses; c) Colutron velocity filter model-600B and d) five-electrode deceleration lens. The deceleration lens, which is housed in the target chamber, will be discussed in a later chapter. The UHV generating system consists of: a) Leybold model-D65B rotary pump; b) Balzers model-TPH510 turbomolecular pump and c) two CTI model-Torr8 cryogenic pumps. Finally, the UHV instrumentation system consists of: a) MDC model-TGT/1518

Figure 1.2 The energy and mass resolved low energy ion beam system at the University of Western Ontario.

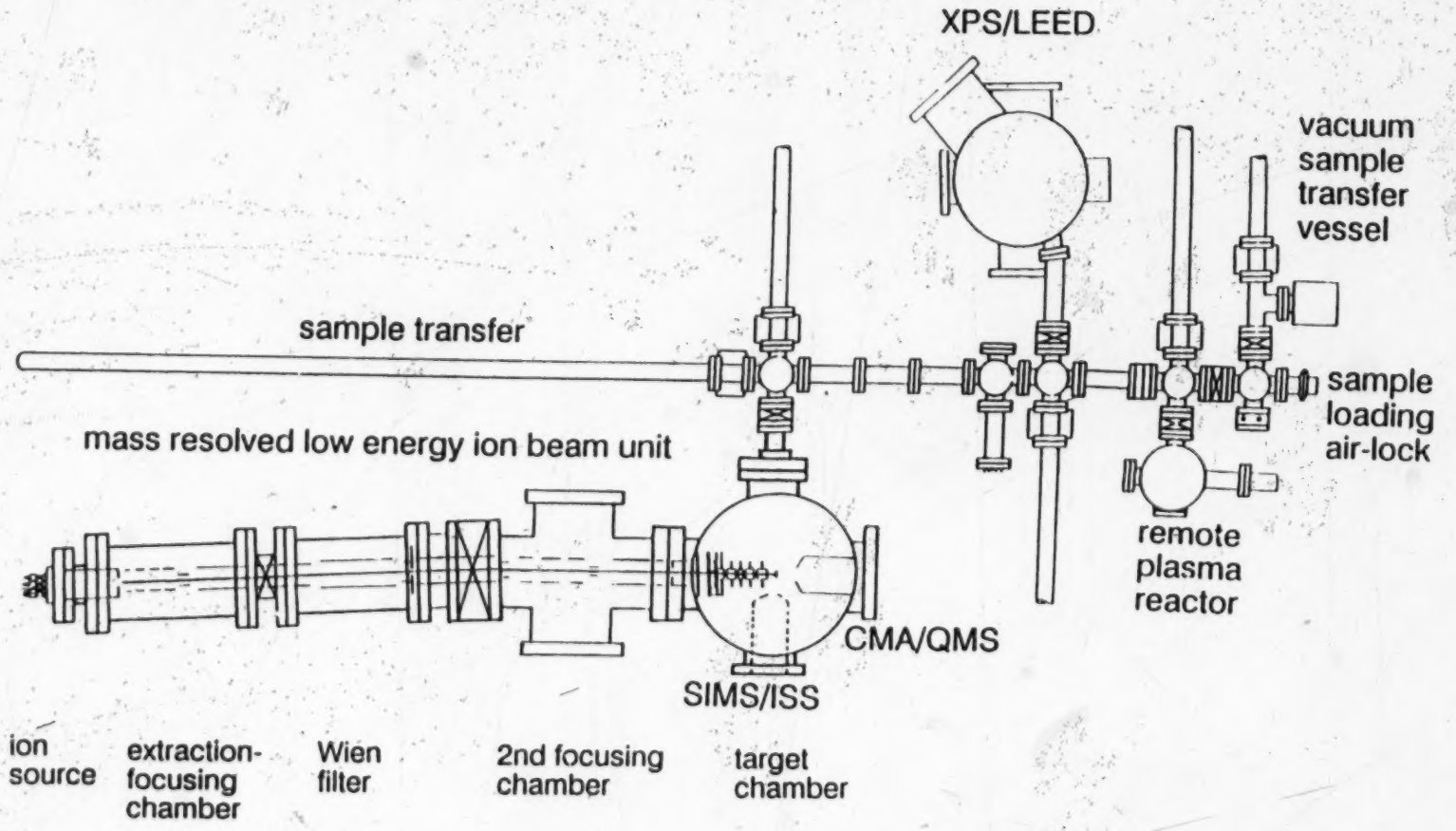

thermocouple gauge; b) two Leybold model-IG3 ion gauges; c) VG SPX-300 quadrupole residual gas analyzer and d) computerized beam profiler. All of the UHV instrumentation equipment will be discussed in this chapter with the exception of the computerized beam profiler.

The LEIBS was designed by W.M. Lau and R.P.W. Lawson. System construction was carried out by X. Feng, S. Sant, I. Bello, G. Good, H. Chen and the author of this thesis. The UHV generating system was assembled by X. Feng, S. Sant and the author. Operation of the quadrupole mass spectrometer and the sample transfer system were verified by S. Sant. I. Bello commissioned the XPS system. The operation of the ion optics, especially the deceleration system, was simulated and verified by the author. Finally, assistance with the electronics and test equipment was provided by R. Schmaus and H. Chen, under the author's direction.

1.2.1 Ion Sources

The ion source is the most important component in all ion beam systems. The type of ion source chosen determines the energy spread and the current density of the beam. For research systems, a current density of microamperes and an energy spread of below 10 eV is usually desirable. For commercial systems, length of time period for the beam operation, high current output ($\approx$ 100 mA), cost of maintenance and operation are also important parameters in selecting a viable ion source.

Of the many existing ion sources, the most commonly used ion source is the hot-cathode source. The two earlier types of hot-cathode sources are Freeman and Sidenius[21] sources. Today, most of the hot-cathode sources are modifications of these two sources. The principle of operation of this type of ion source is fairly simple. A tungsten cathode is usually found in the ionization chamber. The cathode can be placed in a lateral or horizontal position depending on the ion extraction mechanism. When a potential is applied between the anode and cathode, a region of space-charge-limit potential is formed. Electrons by thermionic emission from the cathode are accelerated towards the anode. These energetic electrons interact or collide with the gas in the space-charge-limit potential region to form ions and secondary electrons. As more gas particles are ionized, a cloud of ions and electrons (plasma) is created between the cathode and anode. Ions will move towards the cathode, and electrons will move from the cathode to the plasma (see Fig. 1.3)[22]. The electron current density is given by the Child-Langmuir[23] equation:

$$J_- = (2e/m_e)^{1/2} (V_d^{3/2}/9\pi d_s^2) \qquad (1.1)$$

Similarly, the ion current density is

$$J_+ = (2e/m_i)^{1/2} (V_d^{3/2}/9\pi d_s^2) \qquad (1.2)$$

where m_e and m_i are mass of the electron and ion. V_d and d_s are the potential drop and thickness of the sheath, respectively.

Ions can be extracted from the plasma in two different ways. In the Freeman ion sources, a typical lateral cathode source is used

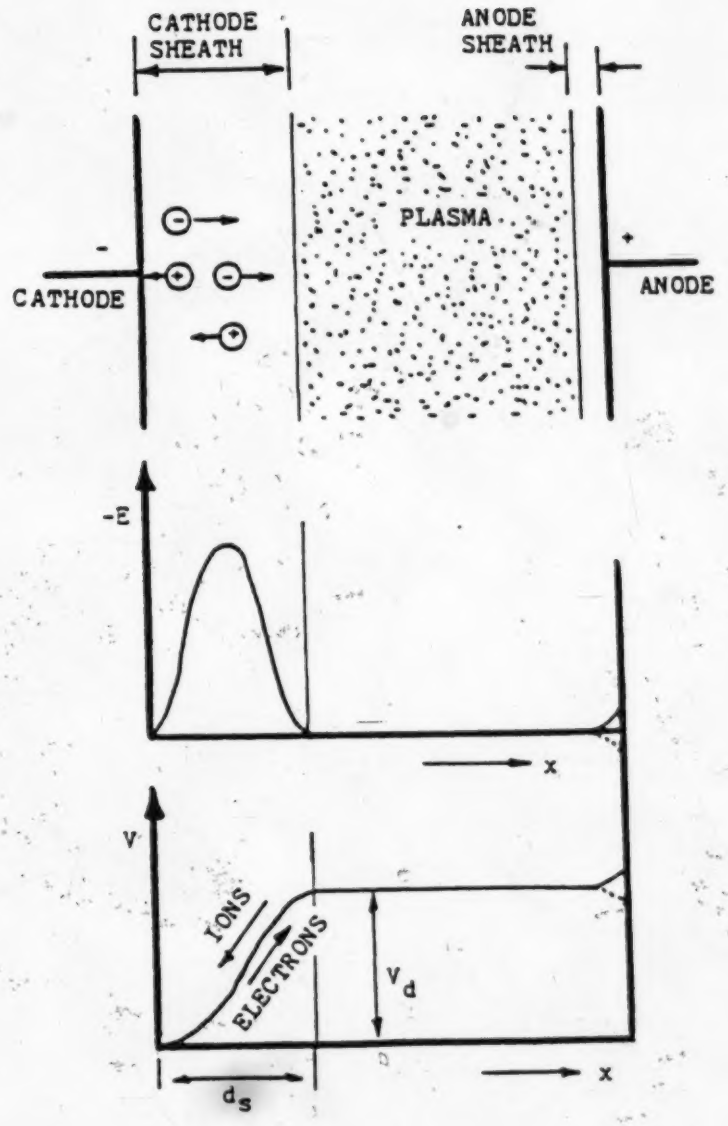

Figure 1.3 Potential and field diagram of the hot cathode electron impact ion source.
(adapted from reference 22, Wilson & Brewer)

which allows ions to be extracted vertically to the axis of the plasma through a slit-shaped aperture. To obtain a strong discharge, the lateral cathode is positioned extremely close to the extraction slit. Because of the large slit, an ion current as high as 100 mA can be extracted. The energy spread of the Freeman source is about 50 eV, and the operating pressure ranges from 10^{-2} Pa to 1 Pa.

Ions are extracted axially from the plasma through a circular aperture in Sidenius ion source. A hollow cathode is placed axially in the ion source. Within the hollow cathode, the high electron density from the thermionic emission maximizes the ionization of the gas. Since the circular aperture is smaller than the slit-aperture, the extracted ion current is in the region of hundreds of microamperes. Despite its compact size, the Sidenius ion source is capable of producing up to 500 μA of Ar^+ at a power consumption of approximately 200 W.

The Colutron model-100[24] ion source and the metal ion source[25] are extensions of the two ion sources described. The glow discharge from the cathode burns towards the anode in a manner similar to that of a Freeman source. Similar to the Sidenius source, the cathode is positioned axially so that the ions are extracted from the circular aperture in the anode. This ion source is fairly easy to maintain and operate at a modest power of approximately 500 W. Currents of Ar^+ beams up to 150 μA can be extracted from these two ion sources. Typical outgassing behavior of the metal ion source is shown in Fig.

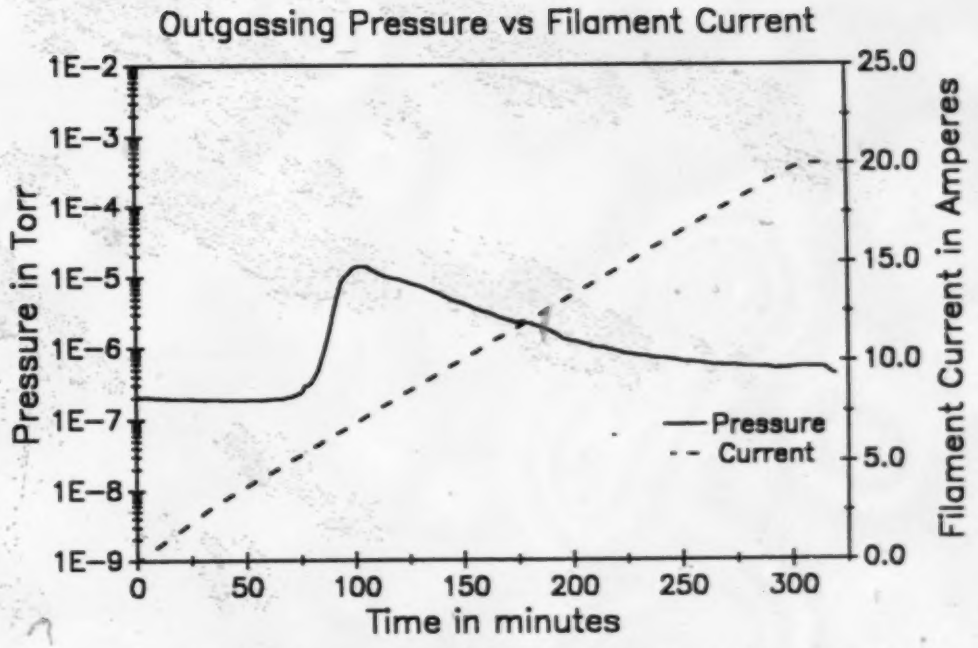

Figure 1.4 Outgassing behavior of a metal ion source (hot cathode electron impact type) as a function of pressure and filament current.

1.4. The ionization filament of the ion source is slowly turned up by a computer to a maximum of 20A over a period of 5 hrs and 25 mins. Filament current will increment only if the recorded pressure is less than the set critical pressure (10^{-3} Pa) to avoid damage to the ion source.

1.2.2 Beam Focusing System

The ions are extracted and accelerated from the ion source, floating at V_{ip}, by an extraction plate. Often, the extracted ion beam is of very high current intensity and also defocused. Therefore, focusing of the beam is necessary, and the ions are focused and collimated by an Einzel lens which is mounted at the exit of the extraction plate. There are two modes of focusing, High-Low-High (HLH) and Low-High-Low (LHL), for the Einzel lens. As such, the energy of the ion beam before entering the lens is always the same as the energy leaving the lens. The ion paths through the HLH and LHL configurations will be shown in a later chapter. The ion beam is well focused before entering the Wien filter in order to achieve high efficiency in filtering. However, the beam contains the ions generated from the plasma in the ion source and so many undesirable species may exist, even though source outgassing is mandatory. These undesirable ion species must be removed to obtain a high quality beam. The Wien filter provided with the Colutron configuration is a "straight-through" filtering system which will be explained below. Often, the beam leaving the Wien filter is defocused because of the filtering effect by the Wien filter. As a result, a second Einzel

lens is placed after the velocity filter to recollect and refocus the mass-filtered ion beam, before final deceleration, to minimize current loss due to defocusing.

1.2.3 The Wein (Velocity) Filter

The detailed specification of the Wien filter can be found elsewhere[20]. The velocity (E x B) filter utilizes the balance of electric and magnetic forces to select or filter out different masses. In a velocity filter, if the magnetic and electric fields are perpendicular to each other, then the resultant force due to the influence of both fields upon a charged particle is

$$qE - q(v \times B) = 0 \qquad (1.3)$$

where **E** is the electrical field strength, **v** is the velocity of the ion and **B** is the magnetic field strength. Since the magnetic field and electric fields are perpendicular, the mass **M** passing undeflected through is given by:

$$M = 2qV(B/E)^2 \qquad (1.4)$$

In the configuration shown in Fig. 1.5, ions having mass M + ΔM will be separated from ions having mass M by a distance D given by[26]

$$D = \frac{1}{2} La \frac{E}{V}\left[\left(\frac{M}{M + \Delta M}\right)^{1/2} - 1\right] \qquad (1.5)$$

Therefore, by altering the magnetic or electric fields, a selected ion species can be separated from an ion beam of mixed species.

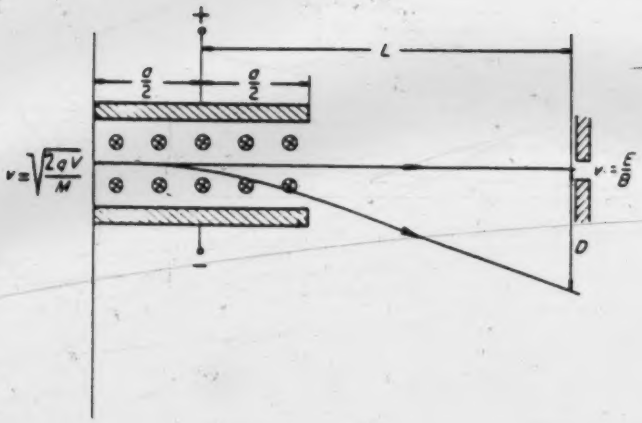

Figure 1.5 Configuration of a Wien (ExB) filter.
(adapted from reference 26, Ryssel and Ruge)

1.2.4 UHV Generation

The initial pumping stage (100,000 - 10 Pa) is handled by a Leybold D65BCS rotary pump. After the initial pumping stage, a Balzers 510 Turbomolecular pump further reduces the pressure. The turbomolecular pump also keeps the pressure of the ion extraction chamber below 10^{-3} Pa range, in order to reduce the formation of neutrals as a result of gas phase neutralization. A CTI CRYOTORR-8 cryogenic pump is placed at the second focusing lens chamber in order to maintain pressure in the low 10^{-6} Pa range. Another CRYOTORR-8 cryopump is used to keep the pressure in the target chamber in the low 10^{-7} Pa region. To further improve the vacuum condition of the system, an orifice is placed at the entrance of the target chamber to provide differential pumping.

1.2.5 Vacuum Gauges

One thermocouple gauge and two ionization gauges are used to measure the pressure of the low energy ion beam system. The thermocouple gauge uses a thermocouple to measure heat loss from a hot filament due to gas conduction, and the rate of heat loss can be converted to a pressure reading. Since the pressure of the gas entering the ion source is fairly high, a thermocouple gauge is placed at the gas inlet point to record the pressure of the gas. Two nude ionization gauges are used to measure the low pressure in the first Einzel lens chamber and the target chamber. For most ionization gauges, the general equation which governs the relationship between pressure, grid current and collected ion current current is given

by[27]

$$P = I_+/(S\ I_-) \qquad (1.6)$$

where I_+ is the collected ion current, I_- is the grid current and S is a sensitivity factor for a particular gauge.

1.2.6 The VG Quadrupole Mass Spectrometer

During the operation of the system, the quality of the vacuum within the ultra-high vacuum target chamber must be determined before the ion beam is applied to the target. Also, it is important to be able to characterize the ion beam in terms of ionic charge content, energy spread and mass purity before depositing the ions on the target. These tests can be performed by a VG SPX-300 quadrupole mass spectrometer which is positioned along the beam axis and behind the target to facilitate beam analysis when the target is moved away from the beam axis. The general operation of a quadrupole mass spectrometer (QMS) has been documented elsewhere[28] and so only a brief analysis will be presented here. The VG SPX-300 quadrupole mass spectrometer houses a cylindrical mirror analyzer (CMA) and four parallel cylindrical rods to facilitate energy and mass analysis. A simple layout of the VG quadrupole mass spectrometer is shown in Fig. 1.6. The filament can be employed depending on the operating mode of the QMS: analyzing external ions or monitoring neutral gas species. The QMS can check the content of the residual gases (neutrals) by switching on the filament which will ionize these gases. The filament should be off while detecting external ions.

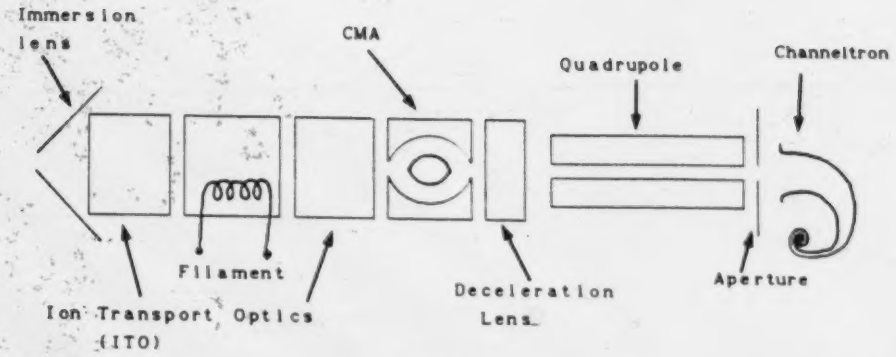

Figure 1.6 Optics assembly of the VG SPX-300 QMS.

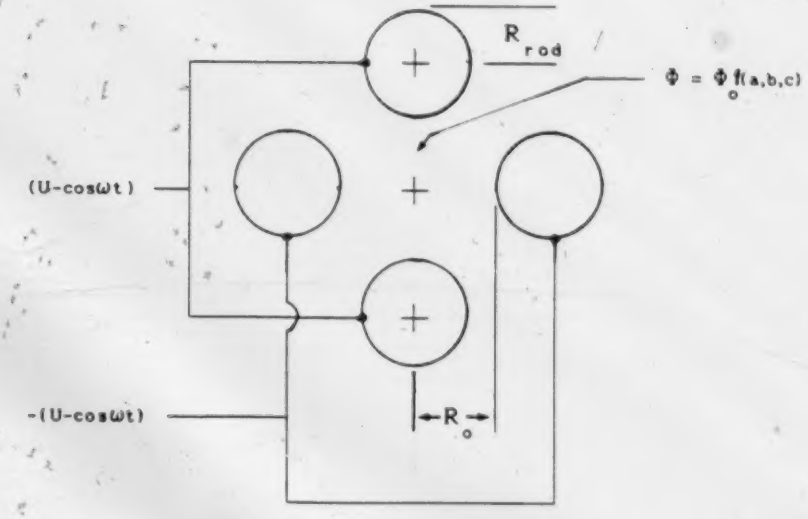

Figure 1.7 Potential in the quadrupole from external supplies.

A cylindrical mirror analyzer (CMA) consists of two concentrical cylinders with a potential difference V across them. The relationship between the energy (E) of the ions passing through the CMA and the potential (V) is given by[29]

$$\frac{E}{eV} = \frac{K}{\ln(R_2/R_1)} \qquad (1.7)$$

where K is a geometrical constant depending on the acceptance angle of the instrument, R_1 is the inner radius and R_2 is the outer radius of the CMA cylinders.

In a quadrupole mass spectrometer (QMS), a D.C. voltage (U) and a sinusiodal voltage, $V\cos(\omega t)$, are superimposed on opposite rods (see Fig. 1.7). The potential distribution in a quadrupole can be expressed by

$$\Phi = \Phi_o(ax^2+by^2+cz^2) \qquad (1.8)$$

where a, b and c are geometrical constants. However, $a + b + c = 0$ in order to satisfy Laplace's equation. $c=0$ since there is no field in the z-direction and $a = -b = 1/(2r_o^2)$. The predetermined voltage on the rods is

$$\Phi_o = U - V\cos(\omega t) \qquad (1.9)$$

The force equations are obtained by substituting Eqn. 1.9 into Eqn. 1.8 and then performing a partial differential on Eqn. 1.8.

$$F_x = -e\frac{\partial \Phi}{\partial x} = -(U - V\cos\omega t)\frac{ex}{r_o^2} \qquad (1.10)$$

$$F_y = -e\frac{\partial \Phi}{\partial y} = (U - V\cos\omega t)\frac{ey}{r_o^2} \qquad (1.11)$$

$$F_z = 0 \qquad (1.12)$$

$$\frac{d^2x}{d(\frac{1}{2}\omega t)^2} + (K_1 - 2K_2\cos\omega t)x = 0 \qquad (1.13)$$

$$\frac{d^2y}{d(\frac{1}{2}\omega t)^2} + [(-K_1) - 2(-K_2)\cos\omega t]y = 0 \qquad (1.14)$$

where $K_1 = \frac{4eU}{m\omega^2 r_o^2}$ and $K_2 = \frac{2eV}{m\omega^2 r_o^2}$

Eqns 1.13 and 1.14 are also known as Mathieu equations[30]. The solutions for these equations are plotted in Fig.1.8. The cross hatched region is the stable region for mass m/e where the trajectory is bounded by x and y forces as time (t) increase to infinity.

In the operation of a QMS, a mass scan starts at the origin and intersects the stable area (see Fig. 1.9), and the condition for this scan line is

$$\frac{k_1}{k_2} = \frac{2U}{V} = \text{constant} \qquad (1.15)$$

The different mass can be scanned by varying U and V but keeping the ratio a constant. From Fig. 1.9, the mass resolution decreases as the mass increases. The mass resolution can be kept constant by rotating

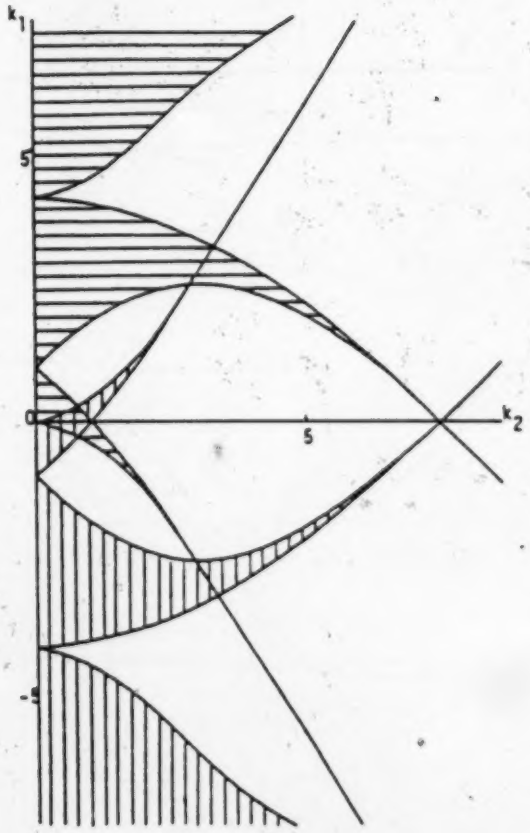

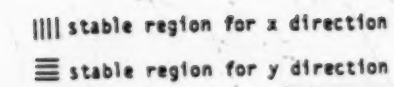

Figure 1.8 Solutions for Mathieu equations.

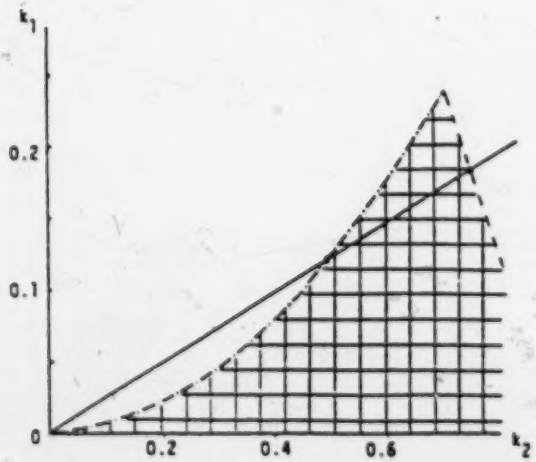

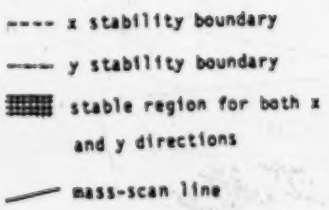

Figure 1.9 Mass scan through the stable region for both x and y directions near the origin.

the line to the apex of the stable region. However, the sensitivity decreases under such an adjustment which is common to quadrupole operation.

Part II Description of the ion optics constructed in this study - the deceleration lens, the beam scanning and profiling unit, and the beam mass-switching unit.

Chapter 2. Deceleration System

2.1 Requirements for the deceleration system

The enlargement of the ion beam diameter due to space charge repulsion during beam transportation is a serious problem in any low energy ion beam system[1]. Such ion beam spreading reduces both the available total current (due to current loss in the ion beam column) and the current density at the target. Since the degree of beam spreading increases with the ratio of radial velocity to axial velocity, optimization of the ion optics for reduction of beam spreading is very critical in the design of lens systems in which ion beams are decelerated before they hit the target. The prevalent approach in designing a low energy ion beam system is to transport the ion beam at energies above a few keV from the ion source, through a mass filter, to a deceleration lens which is mounted in the vicinity of the target in order to reduce the degree of beam spreading between the lens and the target. When the target can be integrated into the deceleration lens as a termination electrode, single step deceleration above the target using near parallel decreasing potential planes is often applied. For example, Armour and coworkers[2] have shown the simulation of such lens operation and have also shown the achievement of little beam spreading down to 1eV at a current density of $10\mu A/cm^2$. When target maneuvering such as tilting is required, the target is normally situated outside the deceleration lens in a near field-free region in order to reduce the effect of

target orientation on the beam shape. The Herman lens, which consists of 13 electrodes, is probably the most elaborate deceleration lens used in a low energy ion beam system[3]. In such a system, a decelerated beam with current density of $8\mu A/cm^2$ at 30eV has been reported. As a simpler approach, Liebl *et al* have used a three-element deceleration lens for beam generation between 50-500eV and obtained $100\mu A/cm^2$ at 100eV[4].

This chapter reports on the design of a deceleration lens with five electrodes to bridge the gap between the Herman lens and the Liebl lens approaches. The lens performance under the two different operation modes, (a) single step deceleration by using only two electrodes and (b) multiple focusing-deceleration by activating all five electrodes, will be discussed.

2.2. Theory

2.2.1 Analytical Methods

The potential at $U(r,\alpha,z)$ in a cylinder can be obtained by directly solving the Laplace's equation:

$$\nabla^2 u(r,z) = \frac{1}{r}\left(\frac{\partial u}{\partial r}\right) + \frac{\partial^2 u}{\partial r^2} + \frac{\partial^2 u}{\partial z^2} = 0 \qquad (2.1)$$

Generally, the solution for Laplace's equation in cylindrical coordinates involves the Bessel function. Therefore, solution for Laplace's equation by solving directly is often time consuming. For

example, if two cylindrical electrodes are separated by a gap, the potential distribution along the gap will generate a complicated set of boundary conditions which will greatly lengthen the steps in obtaining a solution.

The potential within the cylindrical electrode can also be obtained from a charge density method. Briefly, charge distributions on the lens are considered to be the only sources of electrostatic potential in space. As such, the potential V(r) at any point r in multiple cylindrical electrodes can be calculated by superposition of the contribution from each surface charge element $\sigma_i(r_s)$ at a point (r_s) on an electrode i of an N electrode lens:

$$V(r) = \sum_{i=1}^{N} C_i \sigma_i(r_s) \qquad (2.2)$$

where

$$C_i = \frac{1}{4\pi\varepsilon_o} \int_{s_i} \frac{ds}{|r-r_i|} \qquad (2.3)$$

and s is a surface element on the electrode. Since the voltage on each electrode is known, the set of voltages on the lens can be applied as a special case to Eqn. (2.2) for the estimation of the charge distributions. Once these charge distributions on each electrode are known, they can be used to calculate the potential in space for the determination of ion trajectories in the lens.

2.2.2 Numerical Methods

The Laplace equation can be solved numerically by a relaxation scheme. The entire space inside the cylindrical electrode is first partitioned by a mesh of points. Therefore, Laplace's equation is approximated by finite difference equations. From the boundary potential, the potential at any point can be calculated iteratively until the set convergence is reached. Again, the calculation time can be lengthy if the mesh is large, and the accuracy of the result will suffer if the mesh at the gap is insufficiently partitioned.

In this work, the design of the deceleration lens was assisted by an ion path simulation program, CHDEN, which calculates the potential distribution within a lens by a charge density method[5]. The theory and algorithm of the program have been detailed elsewhere[6]. With a slight variation from Eqns (2.2) and (2.3), the numerical solution for potential at $u(r_j, z_j)$:

$$u(r_j, z_j) = \sum_{i=1}^{N} G_{ij}\, \sigma_i \qquad (2.4)$$

where $$G_{ij} = \frac{1}{2\pi^2 \varepsilon_0} \frac{K(\tau_{ij})\, \Delta S_i}{[(r_j + r_i)^2 + (z_j - z_i)^2]^{1/2}} \qquad (2.5)$$

ΔS_i is the area of the i^{th} charge ring and $K(\tau_{ij})$ is the complete elliptical function of the first kind. Detailed expansion of the above equations for numerical computation can be found in M. Szilagyi[7]. Finally, the elliptical function can be approximated by a polynomial of the form[8]:

$$K(\tau) \cong a_0 + a_1\eta + a_2\eta^2 + a_3\eta^3 + a_4\eta^4 + (b_0 + b_1\eta + b_2\eta^2 + b_3\eta^3 + b_4\eta^4)\ln(1/\eta) \quad (2.6)$$

where $\eta = 1 - \tau_{ij}^2$ (2.7)

and $\tau_{ij}^2 = 4r_i r_j/[(r_j+r_i)^2 + (z_j - z_i)^2]$ (2.8)

When space charge effects are required to be included in these calculations, the divergent force due to the space charge is determined by Gauss's law and superimposed onto the forces due to charge on the lens for the estimation of ion trajectories. In the CHDEN program, the radial space charge distribution was assumed to be uniform within the cross-section of the lens. As such, the space charge effect is only approximate and probably under-estimated.

2.3 Designing of the deceleration lens

The ion optics control in the present low energy ion beam system is shown in Fig. 2.1. The target is at ground potential and the anode exit of the ion source is at V_{ip} = 0 - 200V above ground. The later potential determines the impact energy of the ion beam at the target. Normally, the ion beam was transported at $V_B \cong$ 3keV in the flight tube segments of the ion column. The deceleration lens in this work consists of the final five electrodes in front of the target/Faraday cage. In front of the entrance of the deceleration lens is a transfer lens with voltage V_{de} followed by three flight tube electrodes. The transfer lens weakly focuses the incoming beam

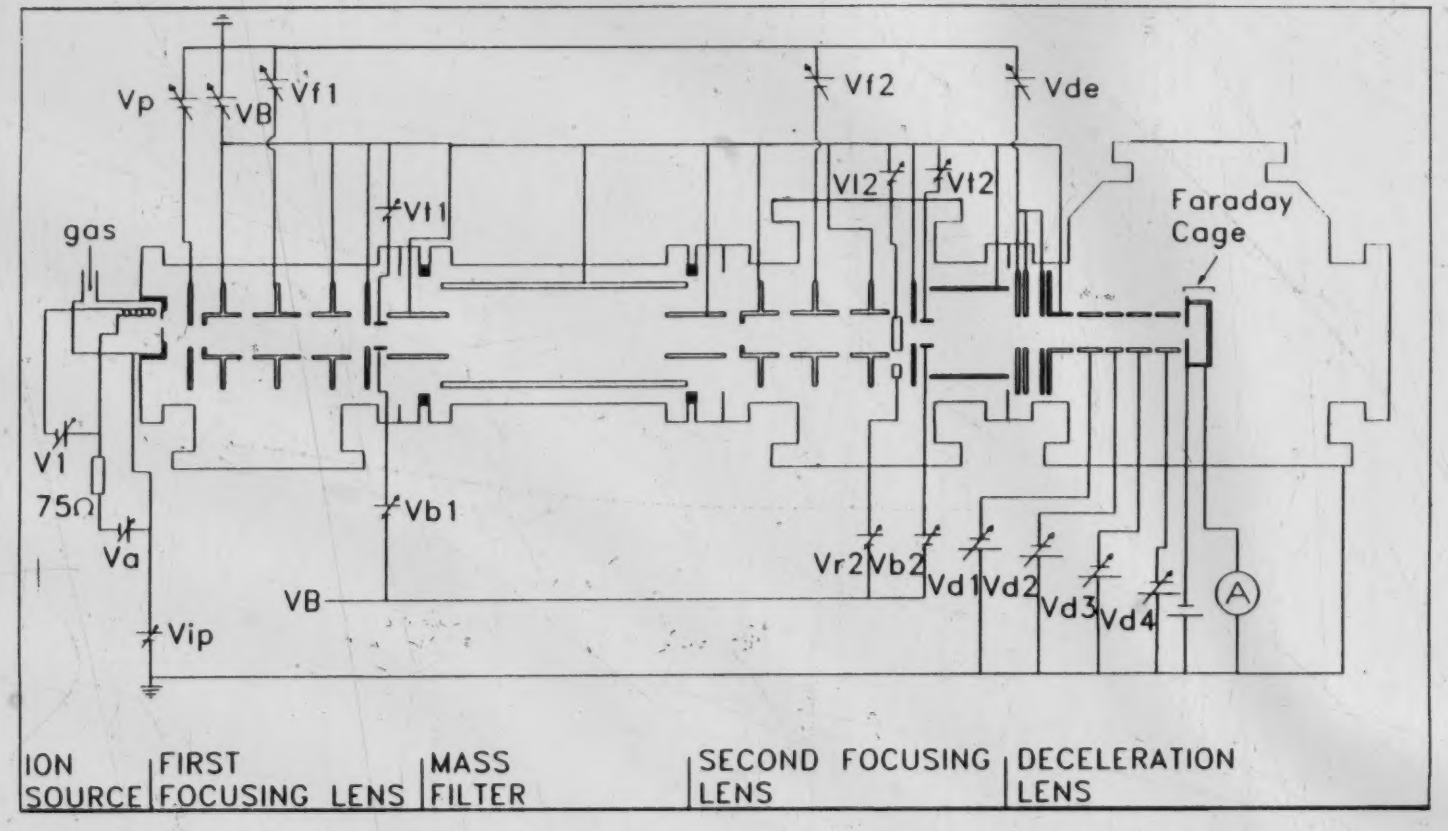

Figure 2.1 Ion Optics Control.

into the deceleration lens. The flight tube electrodes house a permanent ring magnet in order to prevent electrons from entering the deceleration lens. The entrance of the deceleration lens was normally operated at the flight tube potential and the last electrode at -10V. An optional capping electrode at ground potential could be installed for further reduction of field penetration into the target region.

The simulations for the designs of the deceleration lens were performed on a 25 MHz 386 IBM PC with a 80387 math-coprocessor. For 640 KB of RAM, CHDEN permits a maximum of 520 sections for the calculation of charge distribution matrix. Therefore, accuracy on the numerical calculation of the charge distribution depends on the computer memory. The end product, an inverted coefficient matrix, can be converted to provide information on potential and electrostatic field distributions. CHDEN allows a maximum of 10 electrodes to be included for lens simulation which prevents a complicated lens configuration from being simulated. A maximum of 10 initial ion trajectories can be set up to perform the ray tracing.

Using the computer configuration mentioned, a typical simulation with 200 matrix sections, space-charge effect and three ray tracing took approximately 10 minutes. Simulations were initiated with the three-electrode Einzel lens, the most basic geometry, with HLH and LHL focusing. A basic understanding of these two focusing modes leads to the construction of the more complicated deceleration lens. Samples of the ray tracing outputs are shown in Fig. 2.2a and

Fig. 2.2b. The focusing effect can be explained by the superimposed potential contours (100 V/line), which were obtained by a relaxation algorithm, on the ray tracing outputs. From the potential contours, the electric field can be obtained and the force on the charged particle can be obtained by

$$\mathbf{F} = q\mathbf{E} \qquad (2.9)$$

The merging of the HLH and LHL focusing modes led to the design of a compact five-electrode lens which can be fitted into the target chamber. The simulation began with a five-electrode lens of equal length and radius. Initial trajectories for the ions, A..D, used in the simulation were: A) 0° and $r/r_o = -0.2$; B) -0.5° and $r/r_o = 0$; C) 0.5° and $r/r_o = 0$ and D) 0° and $r/r_o = 0.2$. r_o ($d_o/2$) is the common radius of each electrode and different voltages were applied to the electrodes. The optimized deceleration voltages on the electrodes for different set of lens' entrance voltages, 3kV, 5kV, 7kV, 9kV and 10kV can be obtained from the minimum beam diameter at the exit of the lens (d'). These sets of voltages are summarized in Table.2.1. The d' of ions A-D and B-C for various electrode-voltages were recorded and summarized in Fig. 2.2c. Using these sets of optimized deceleration voltages, the length of each electrode was varied in trying to further reduce d'. Many length configurations were simulated and d' from the deceleration lens with optimized focusing-voltages and electrode-lengths were summarized in Fig.2.2c. The length of each electrode for the deceleration lens will be given in section 2.4.

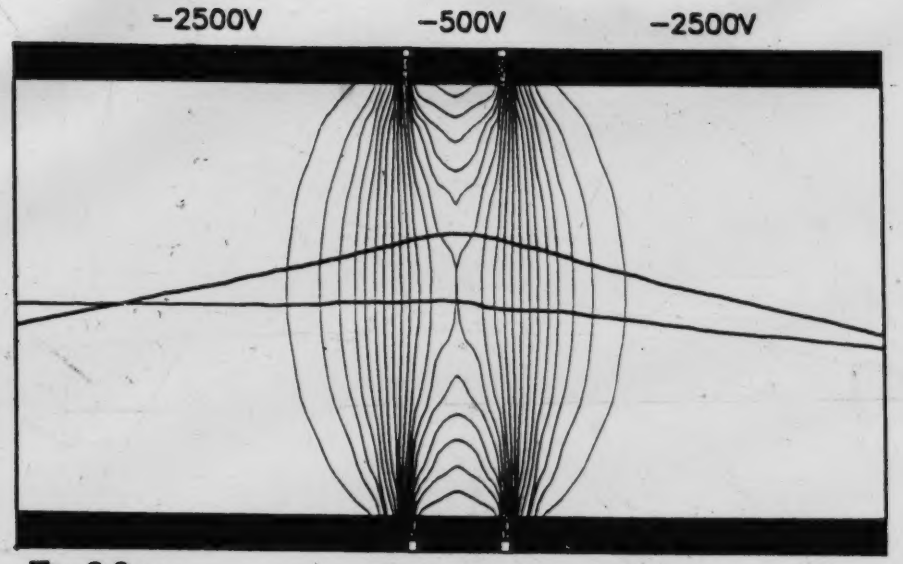

Fig. 2.2a

ION BEAM PATHS

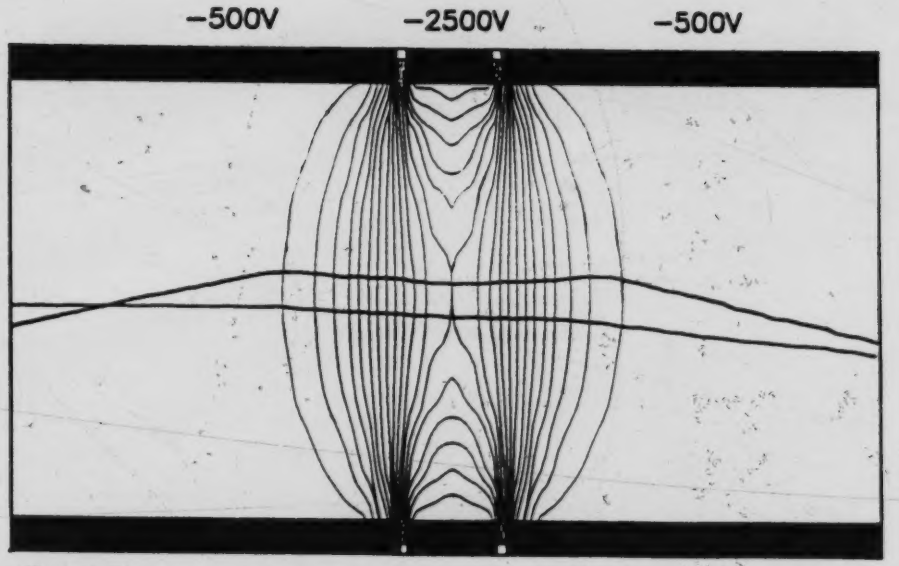

Fig. 2.2b

Figure 2.2. Ion paths and potential gradients to illustrate: (a) HLH focusing mode; and (b) LHL focusing mode.

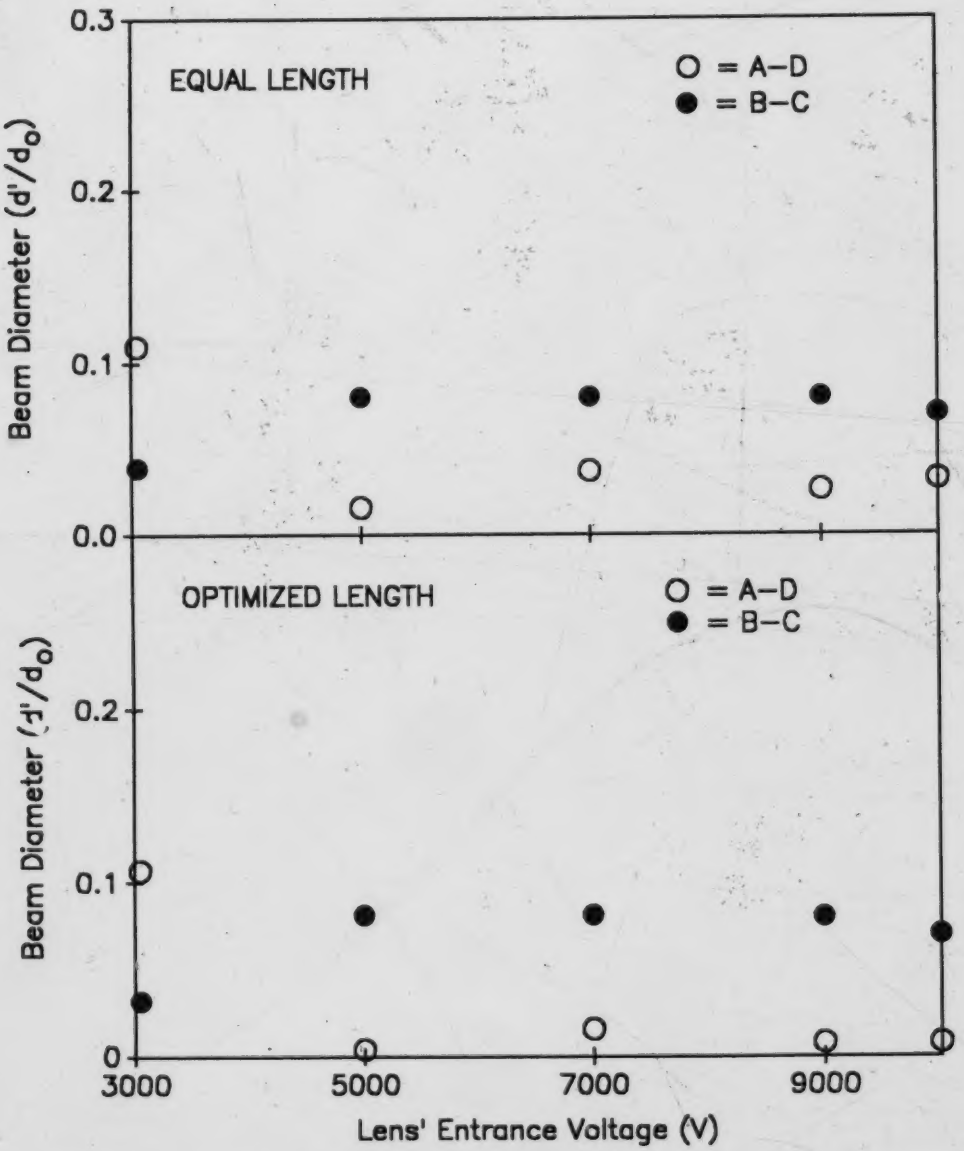

Figure 2.2c Beam diameters of electrodes with equal and optimized lengths.

Entrance Voltages(VB)	(Vd1)	(Vd2)	(Vd3)	(Vd4)
-3000V	-200V	-3000V	-200V	-10V
-5000V	-700V	-5000V	-700V	-10V
-7000V	-1200V	-7000V	-1200V	-10V
-9000V	-1800V	-9000V	-1800V	-10V
-10kV	-2000V	-10kV	-2000V	-10V

Table.2.1. Sets of deceleration voltages used to determine the optimized lengths.

This lens is able to operate either in a simplified mode where a single step deceleration is applied before the exit electrode, or in a full performance mode where the first three electrodes are used as a strong focusing lens to provide a convergent force to counteract the divergent force due to space charge repulsion in the deceleration zone before the exit electrode. The simulated ion trajectories under these two modes of operation are summarized in Fig. 2.3a and Fig 2.3b. With the superimposed potential contours, the paths taken by the ions can be realized. The field densities of Fig. 2.3a and Fig. 2.3b are 150 V/line and 200 V/line respectively. The ions were assumed to be generated at ground potential and had a kinetic energy of 10eV at the exit of the deceleration lens. In the simulation of the space charge effect as included in the results shown in Fig. 2.3a, CHDEN assumes a uniform current distribution inside the lens. In the present experimental setup, beam monitoring indicated that the typical argon ion beam input to the deceleration lens had a beam current of about 10μA with a beam diameter of about 2mm. A more

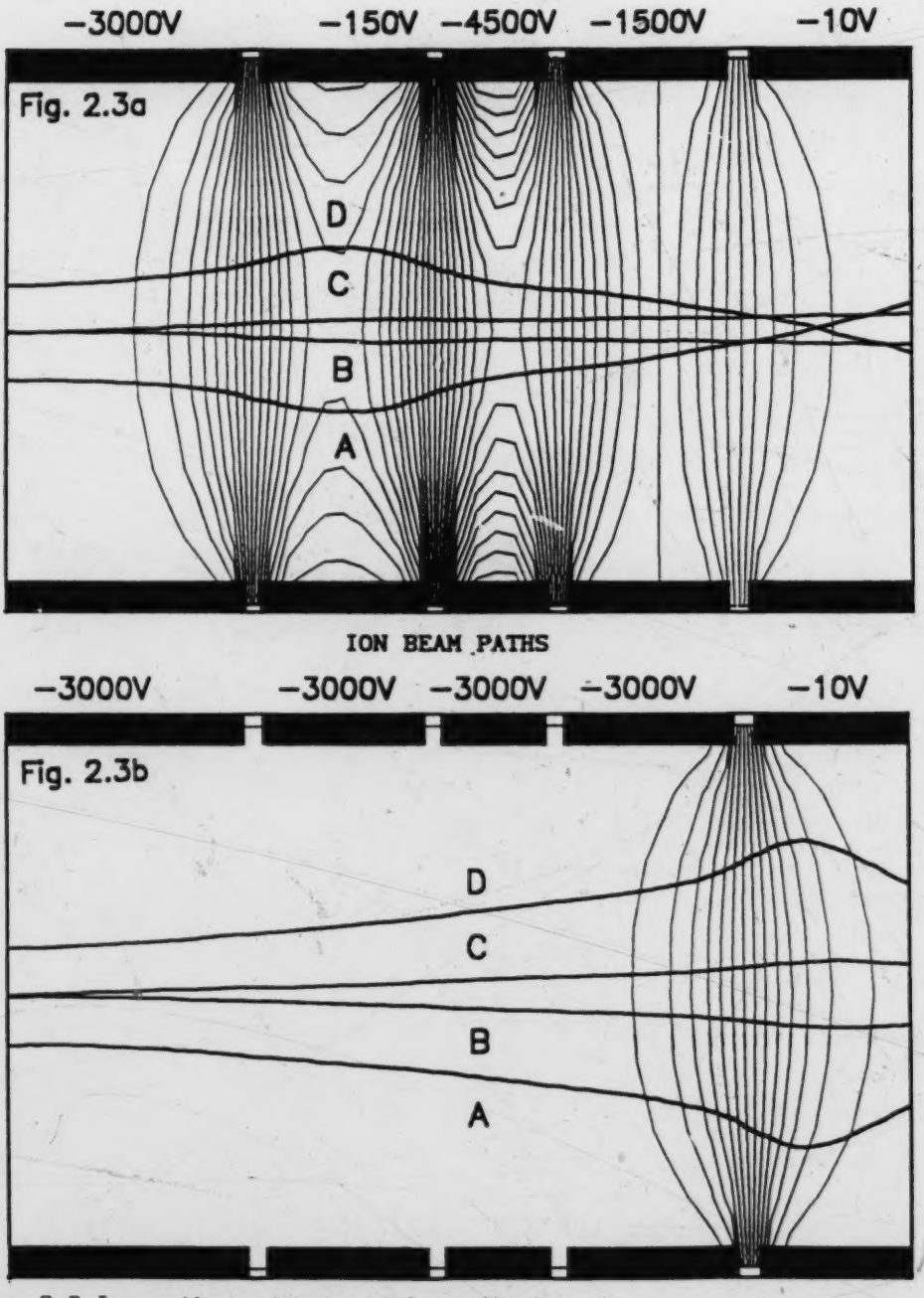

Figure 2.3 Ion paths and potential gradients:
(a) five-electrode focusing mode,
(b) Single-step deceleration.
Common radii of the cylindrical lenses, r_o = 10mm.
Rays A, D represent a parallel, axial beam with r/r_o = 0.2;
Rays B, C represent a divergent, axial beam with r/r_o = 0 and half-angle divergence $\theta = 0.5^{\circ}$.

realistic estimation of the space charge effect was performed by calculating the beam spreading of the focused argon ion beam in the flight tube of the ion column (at 3kV) using the analytical equations and numerical data published by Nagy *et al*[1]. The total current input to CHDEN was then adjusted until its prediction of beam spreading of argon ions originating at about 1mm off axis coincided with that obtained by Nagy's method. The resultant beam trajectory prediction, as shown in Fig. 2.3a, indicates that when all five electrodes of the present deceleration lens system were activated in a focusing-deceleration mode, beam divergence due to space charge repulsion can be reduced by converging the beam into the deceleration zone.

2.4 Construction

The deceleration lens design is detailed in Fig. 2.4. The lens electrodes are each of 20mm diameter and of lengths: B =30 mm; D1 = 15mm; D2 = 10mm; D3 = 20mm; and D4 = 20mm. The gap, G, was chosen to be 5mm wide to avoid dielectric breakdown. The entrance electrode, B, is connected to the beam transport voltage power supply, V_B. The D1-D4 electrodes are controlled by V_{D1}-V_{D4} respectively. In the single-deceleration mode, all electrodes were connected to the beam transport voltage except the last electrode, D4, which was set at -10 to -20V. In the focusing-deceleration mode, B - D2 were configured as a strong focusing lens with D3 and D4 as deceleration electrodes. In this operation, V_{D1} was changed from 0 to -2000V and V_{D2} from 0 to -5000V for converging the incoming beam. Finally, V_{D3} (0 to -2000V)

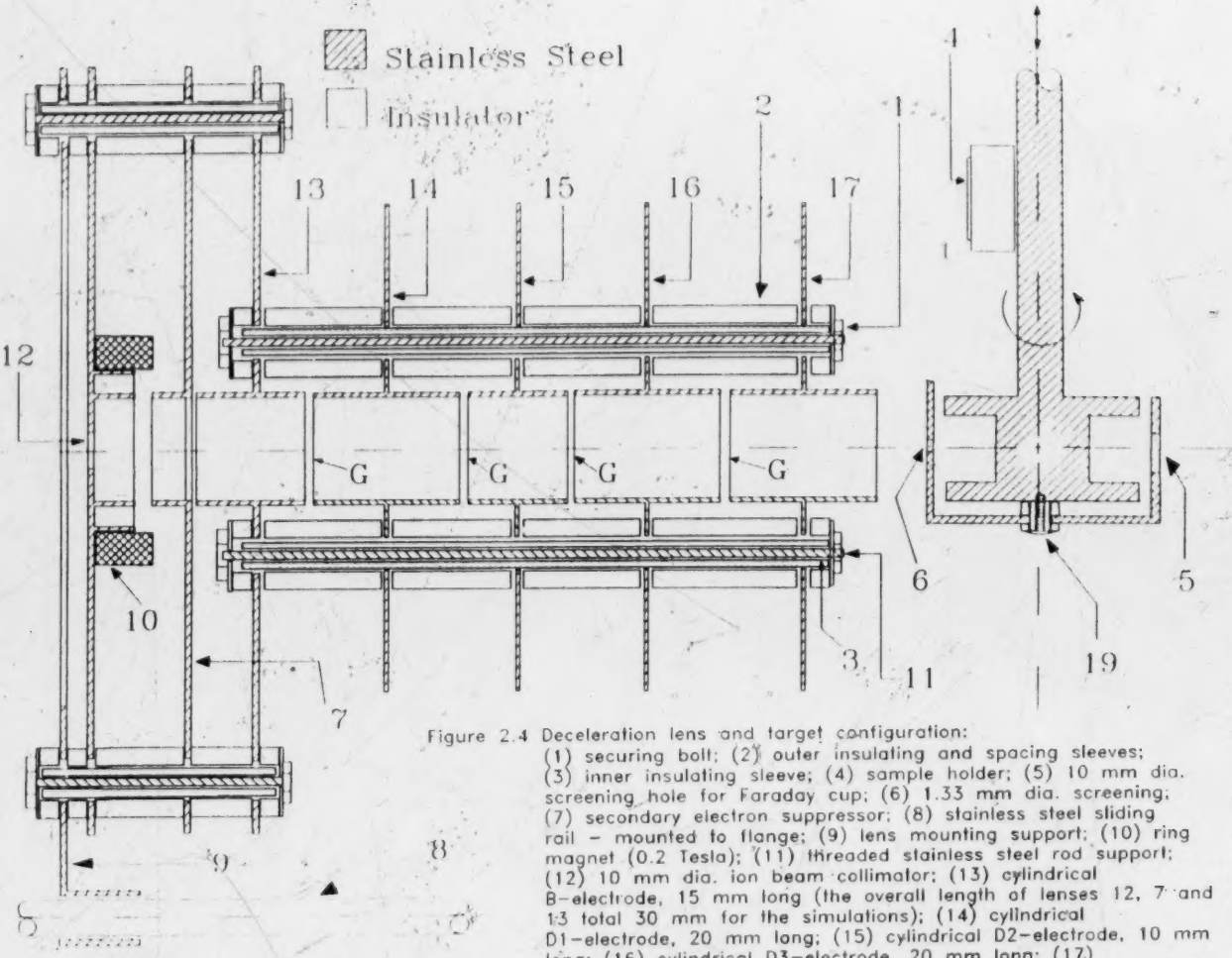

Figure 2.4 Deceleration lens and target configuration: (1) securing bolt; (2) outer insulating and spacing sleeves; (3) inner insulating sleeve; (4) sample holder; (5) 10 mm dia. screening hole for Faraday cup; (6) 1.33 mm dia. screening; (7) secondary electron suppressor; (8) stainless steel sliding rail – mounted to flange; (9) lens mounting support; (10) ring magnet (0.2 Tesla); (11) threaded stainless steel rod support; (12) 10 mm dia. ion beam collimator; (13) cylindrical B-electrode, 15 mm long (the overall length of lenses 12, 7 and 13 total 30 mm for the simulations); (14) cylindrical D1-electrode, 20 mm long; (15) cylindrical D2-electrode, 10 mm long; (16) cylindrical D3-electrode, 20 mm long; (17) cylindrical D4-electrode, 20 mm long; (18) lens spacing G, 5 mm; and (19) screw.

and V_{D4} (0 to -20V) served to decelerate the beam.

2.5 Evaluation of the deceleration lens

Beam characterization was carried out by using a Faraday cage with a 100 mm^2 or 1.3 mm^2 screening-hole. The Faraday cage was grounded through the microammeter. To measure the total beam current, the large hole (100 mm^2) was used. The ion beam was then focused into the small hole to obtain information on the current density. Beam profiles were generated by moving the small Faraday cage mechanically using a vacuum manipulator or a computerized beam profiler. The details of the beam profiler will be given in chapter 3.

During lens evaluation, the beam extraction chamber (see Fig. 2.1) was at 8 x 10^{-4} Pa, and the Ar gas pressure in the grounded ion source was kept constant at 3.5 Pa. With these conditions, the Ar^+ ions were extracted with a circular plate at a potential of -3 kV. The extracted ions were focused by the Einzel lenses and purified by the mass filter. Then, the Ar^+ ions were brought into the target chamber by a weak transfer lens controlled by V_{de}. The working pressure at the target chamber was at about 1x10^{-6} Pa. When all the deceleration lens electrodes and Faraday cage were connected to the beam transport voltage, a 3 keV argon beam of about 10μA with a beam diameter of less than 2mm was obtained. The beam profile was monitored either by mechanically moving the small Faraday cage or by beam scanning using a computer. The techniques of beam profiling will be further discussed in chapter 3.

In the single-deceleration mode, a well focused beam was observed when the beam energy was above 100eV at the grounded Faraday cage. Below that, beam spreading was evident. The maximum current density as a function of the final beam energy is shown in Fig.2.5. In comparison, the available current density was much higher when the focusing-deceleration mode was applied. Under this mode of operation, the optimal lens voltages were searched using the simulation results (Fig. 2.3) as a guide. In Fig 2.6a, the voltage on D3 electrode was fixed at -1210V and adjustments were made on V_{d1} and V_{d2} until a maximum current was recorded by the Faraday cup. Fixing the best V_{d1} (-170V) obtained from Fig. 2.6a, V_{d2} and V_{d3} can be optimized. With the optimized V_{d2}, values of V_{d1} and V_{d3} can be further optimized. The optimization results are summarized in Fig. 2.6. The beam profile of a typical argon ion beam decelerated to 100eV, obtained by a vacuum manipulator and with the optimal lens voltages, is shown in Fig. 2.7. The decelerated beam had a symmetrical Gaussian-like shape with a beam diameter at half current maximum of about 1.2mm. The current density at the current maximum was about $120\mu A/cm^2$.

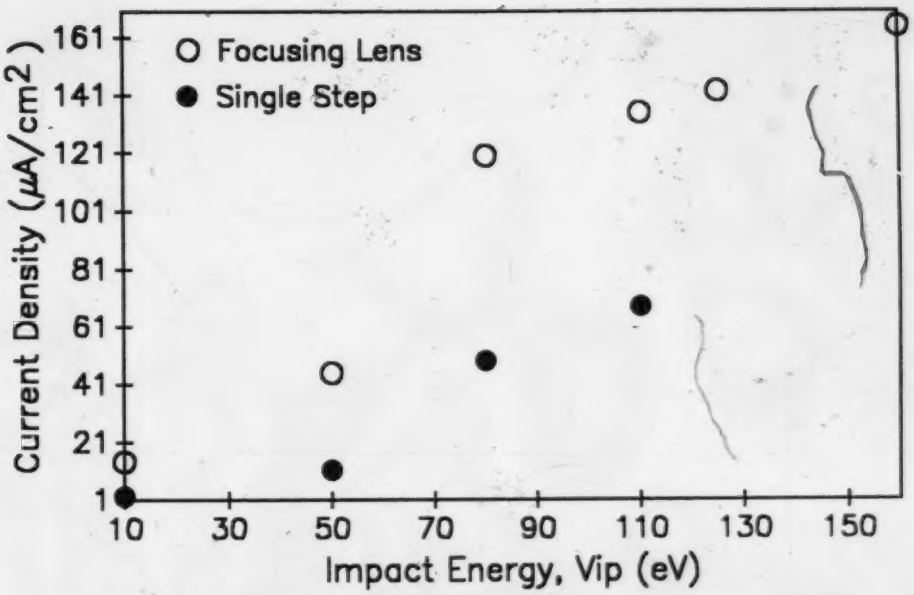

Figure 2.5 Ar^+ beam current density at the target as a function of beam energy for the two deceleration lens configurations.

Fig. 2.6a

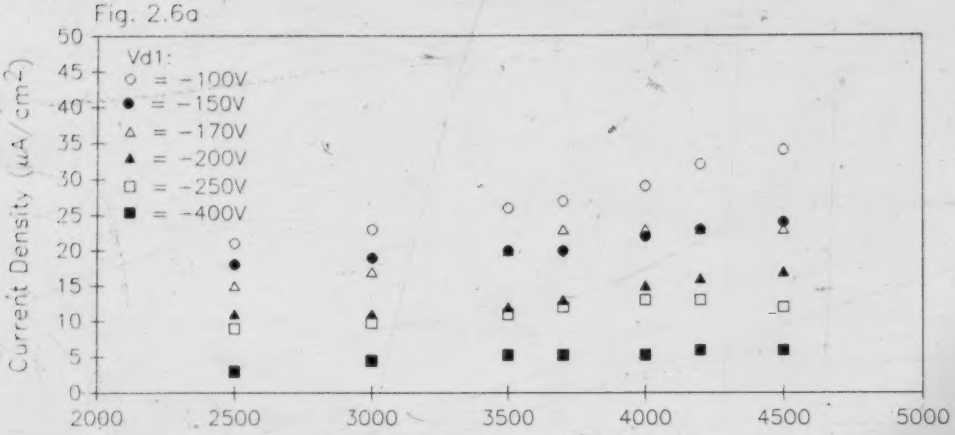

Fig. 2.6b

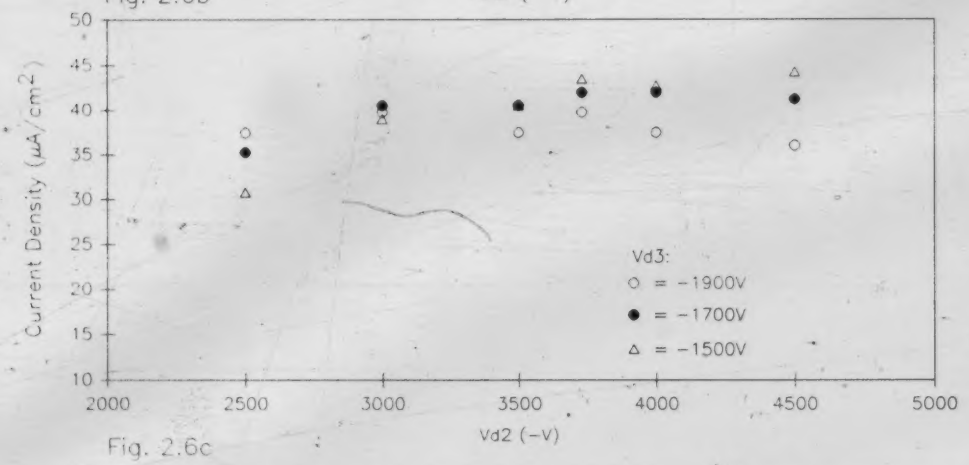

Fig. 2.6c

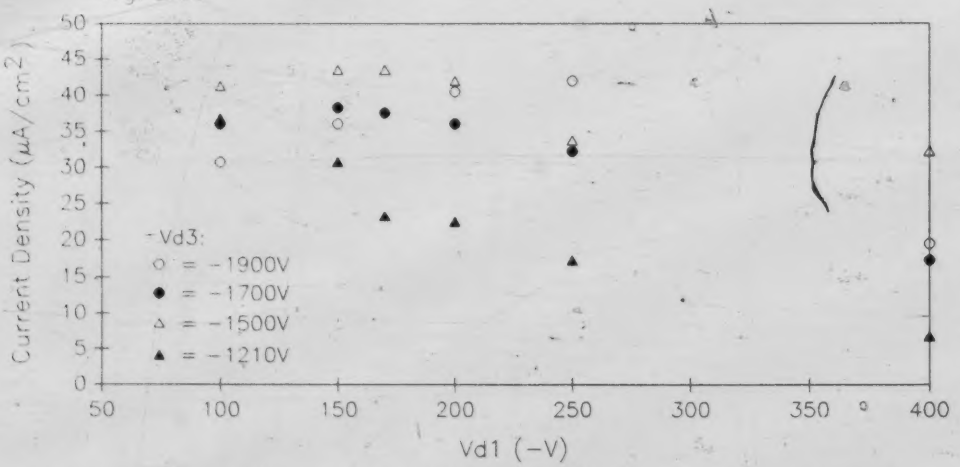

Figure 2.6 Ar^+ beam current density at the target for various optimum lens voltages configurations :
(a) with D3 fixed at −1210V; (b) with D1 fixed at −170V; and (c) with D2 at −3730V.

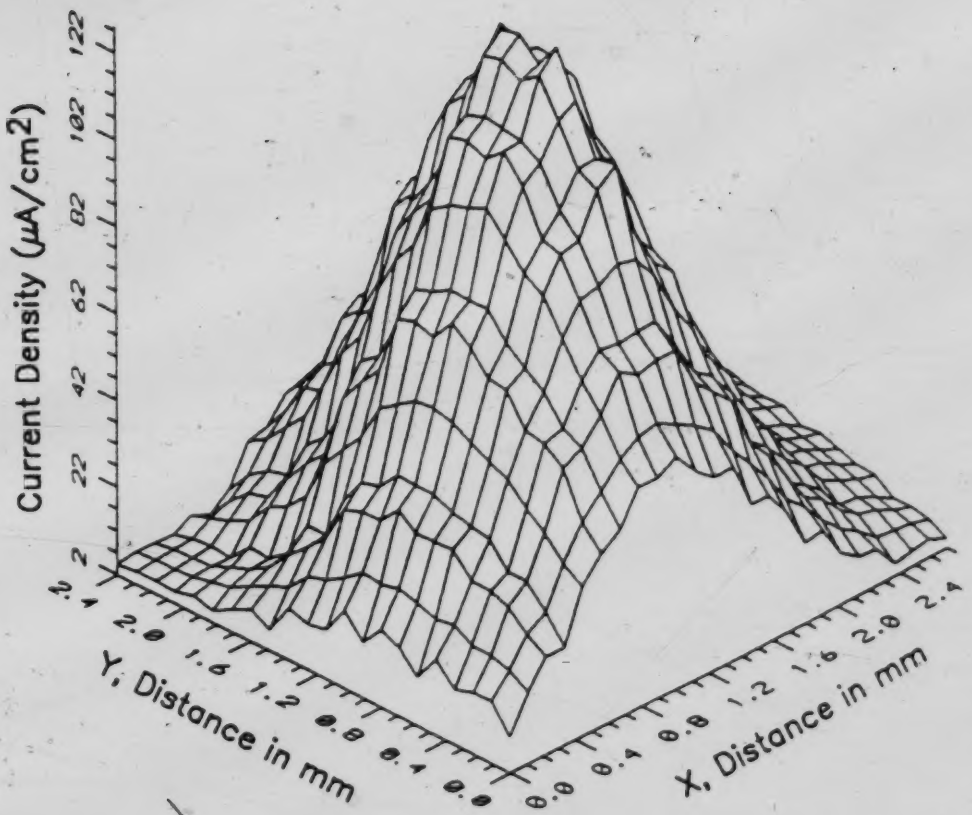

Figure 2.7 Ar^+ beam profile at 100 eV beam energy.

Chapter 3. Rastering and Profiling System

Applications of ion beams in modern surface science research and in microelectronic process technology require the determination of the shape and size of the beam[1,2]. A Gaussian shaped beam profile is often assumed for a well-focused beam. However, the actual beam profile can be determined experimentally by mechanical means in which the beam is focused into a small screen hole or slit of a Faraday cage where a portion of the beam is measured. A two dimensional current intensity map, i.e. the beam profile, can be generated either by moving the Faraday cage or by rastering the beam horizontally and vertically.

For most ion beam systems, the uniformity of the ion dose within a desired bombardment area is critical. In the absence of beam rastering, the ion beam can be defocused to adjust to the bombarded area but the beam profile will at best remain as a Gaussian shape[3]. Rastering or sweeping of a well-focused beam is therefore the best approach for any ion beam experiments when dose uniformity is required. In this approach, an accurate measurement of the beam profile allows the determination of the minimum rastering area which is important when a high total dosage is required over a target area larger than the beam cross section. To demonstrate the importance of the effect of beam size on time, a graph of monolayer vs time is shown in Fig. 3.1. The time for a particular dosage is given by[3]

$$t = \frac{dq}{j} A \qquad (3.1)$$

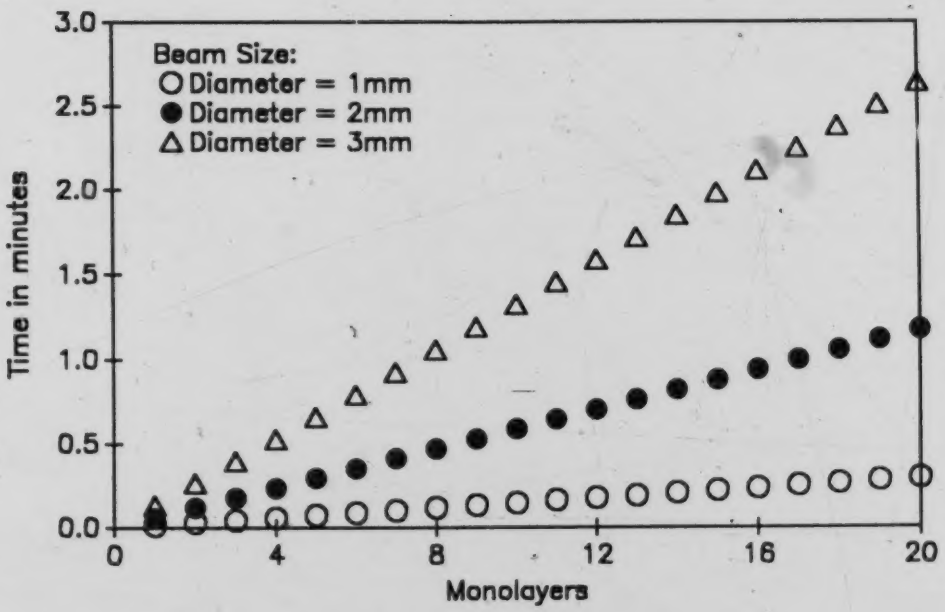

Figure 3.1 Deposition time and thickness (monolayers) as a function of different beam diameters.

where d is the dosage in number of particles per cm^2, q is the elemental charge, j is the current density of the ion beam, and A is a ratio of the rastered area over the beam size. For values in Fig.3.1, A is set at 1, the total beam current is set at 1.0μA with one monolayer equals to $7x10^{14}$ particles per cm^2.

This chapter reports a computer technique which can be implemented to determine the beam profile and to obtain beam rastering. The deflection system consists of two horizontal plates and two vertical plates which serve to steer the beam independently in both the x and the y directions. An IBM PC computer is used to control the beam rastering and to monitor data acquisition. The electrical block diagram of the system can be found in Fig. 3.2.

3.1 Specification

The rastering design must be able to accommodate beam profiling. In most conventional rastering systems, a fixed timing base is usually employed to keep track on the frequency of the rastering voltage applied on the deflector. Because of the fixed timing base, synchronization with a digitizing unit can be difficult although obtaining a beam profile is not entirely impossible. Furthermore, modification of the timing base in order to synchronize with a digitizing unit can be expensive.

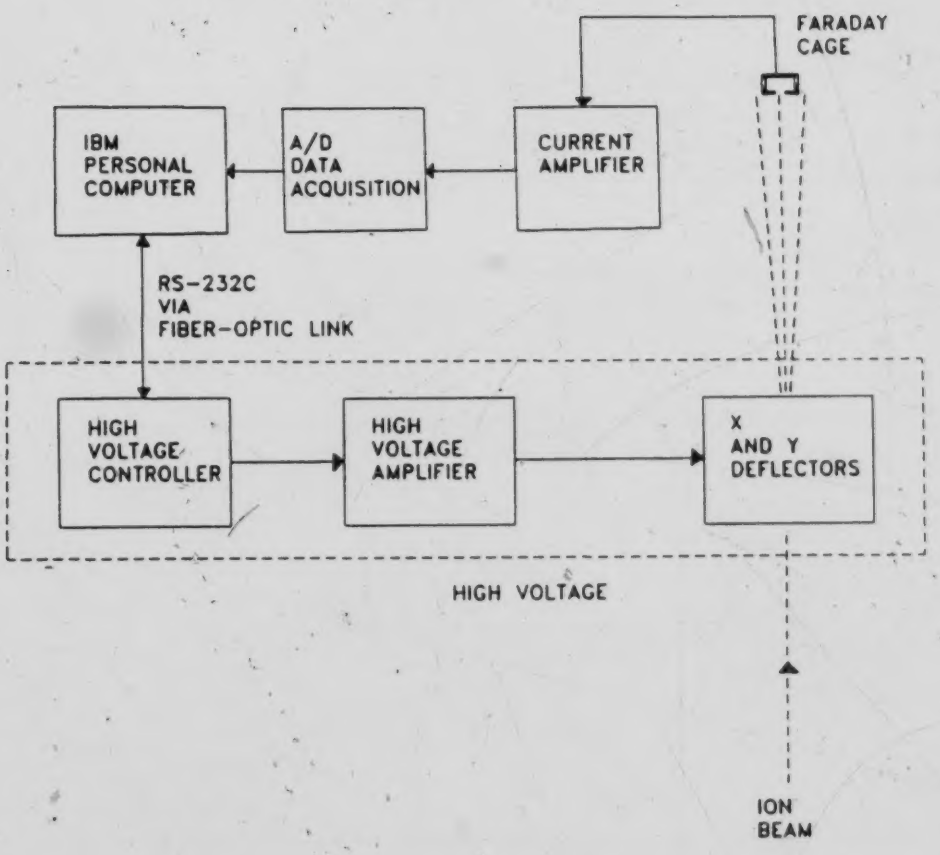

Figure 3.2 Electrical block diagram of the beam profiling and rastering system.

The approach adopted in this study is to develop a cost effective computer technique to implement both rastering and beam profiling techniques. The fixed timing base in conventional methods can be replaced with a flexible timing base implemented by software. Therefore, it is best to have a software which can be used to control the amplitude and frequency of the rastering voltage. The voltage amplitude control offered by the software can be used to compensate the fixed dimension of the vacuum chamber which housed the deflection system. In general, the deflection of a beam by parallel plates, similar to the one in Fig. 3.3, is given by

$$D = L \frac{a}{2d} \frac{V_d}{V_a} \qquad (3.2)$$

where L, a and d are geometrical factors. L is the distance between the deflection system and the target, a is the length of the plates, d is the distance between the plates, V_d is the voltage between the plates and V_a is the acceleration voltage of the beam. With the present configuration, Eqn.3.2 can be further simplified to

$$D \approx 25 \frac{V_d}{V_a} \quad \text{cm} \qquad (3.3)$$

V_a is usually fixed at a particular value (e.g. 3.5kV), and by varying V_d with software, D is changeable and therefore, beam rastering is achieved. The maximum value for V_a is 5kV and for V_d is 200V. Therefore, the attainable rastering distance (D) for these voltages is approximately 1 cm.

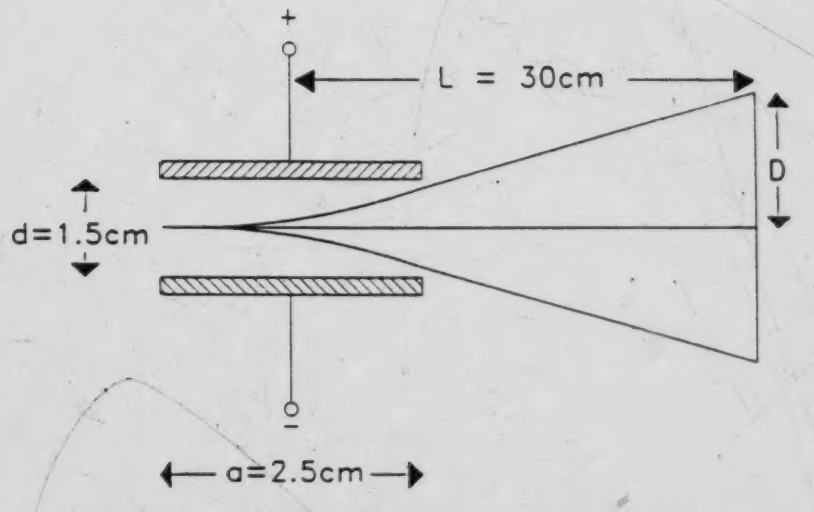

Figure 3.3 Physical layout of a beam deflection system.

3.2 Electronics Design

A computer program, written in Turbo Pascal, has been written and used to control and monitor the beam deflecting operation. The computer communicates with the high voltage controller via a Rs232C optical fiber-link operating at 4800 baud. The transmitted data consist of two parts: a) D/A address and b) output data. Two Motorola communication IC's (Mc14469)[4] at the high voltage controller receive the transmitted data from the computer. The address data are decoded by the address decoder to select the appropriate D/A. Then, the output data are sent to the selected D/A converters (AD7226)[5]. A complete schematic of the high voltage controller is shown in Fig. 3.4a. The outputs from the D/As are buffered before sending out to the high voltage amplifier. The high voltage amplifier schematic diagram for the top deflection plate is shown in Fig. 3.4b. The voltages on each of the other three deflection plates are controlled by identical circuits. The DC component on the deflector is used to position the beam before rastering. The ion beam current collected by the Faraday cage with a small screened hole is amplified and then digitized by the computer. Since the deflection voltages are controlled by the computer, the digitized current can be mapped to form a beam profile. However, if beam profiling is not required, the ion beam is rastered over a sample instead of a Faraday cage. Since the x and y voltages are controlled by the computer, the frequency of the rastering is programmable and does not require a dedicated timing unit.

(A)

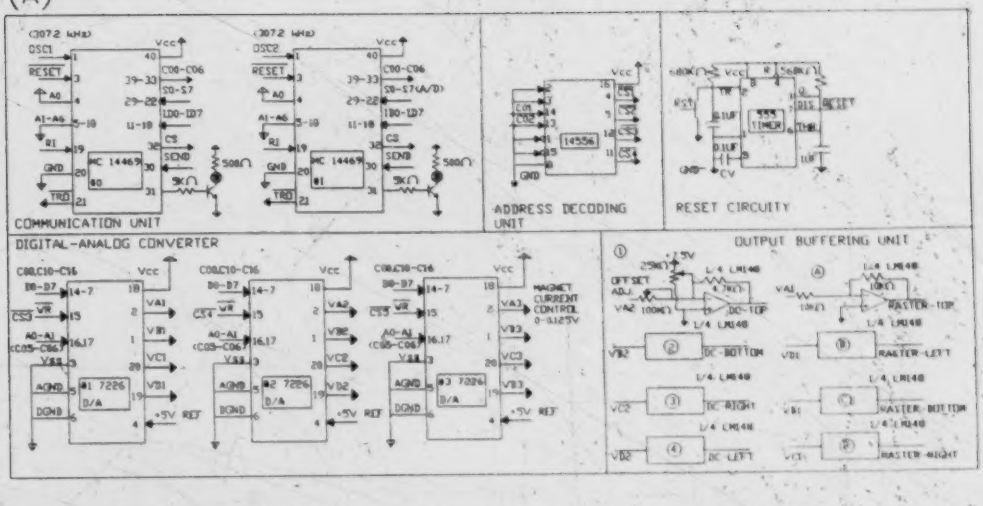

(B)

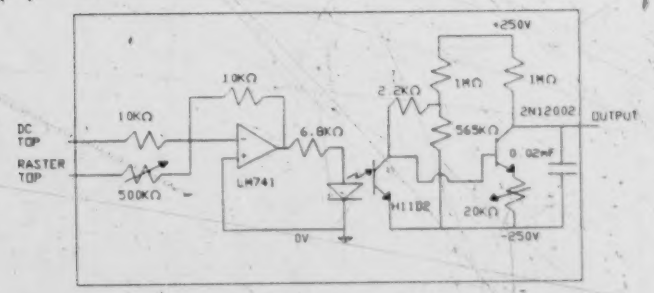

Figure 3.4 Schematic diagrams of: (a) High Voltage Controller; and (b) optical isolated High Voltage Amplifier.

3.3 Evaluation

A computerized beam rastering and profiling system was constructed based on the above specification. The rastering capability of this system was evaluated by depositing In^+ on Si(100). Results on the thickness of the deposited film by rastering will be discussed later. The designed system was also used to obtain profiles of In^+ and N_2^+ beams at impact energy of 50eV. The beam transport voltage, V_a, was fixed at 3.5kV and the deflection voltage, V_d, was at 160V. From Eqn. 3.3, the beam movement (D) is approximately 1.14 cm. Based on the above experimental conditions, profiles of N_2^+ and In^+ were digitized successfully and they are showed in Fig. 3.5a and 3.5b respectively. The maximum beam intensity for both beams is about $28\mu A/cm^2$. The width of the In^+ beam at FWHM is approximately 1.9mm and for N_2^+ beam, the width is about 1.2mm. With the availability of the beam size information, the time required (see Fig.3.6) for a particular dosage over a rastered area can be predetermined accurately.

(a)

5 mm

(b)

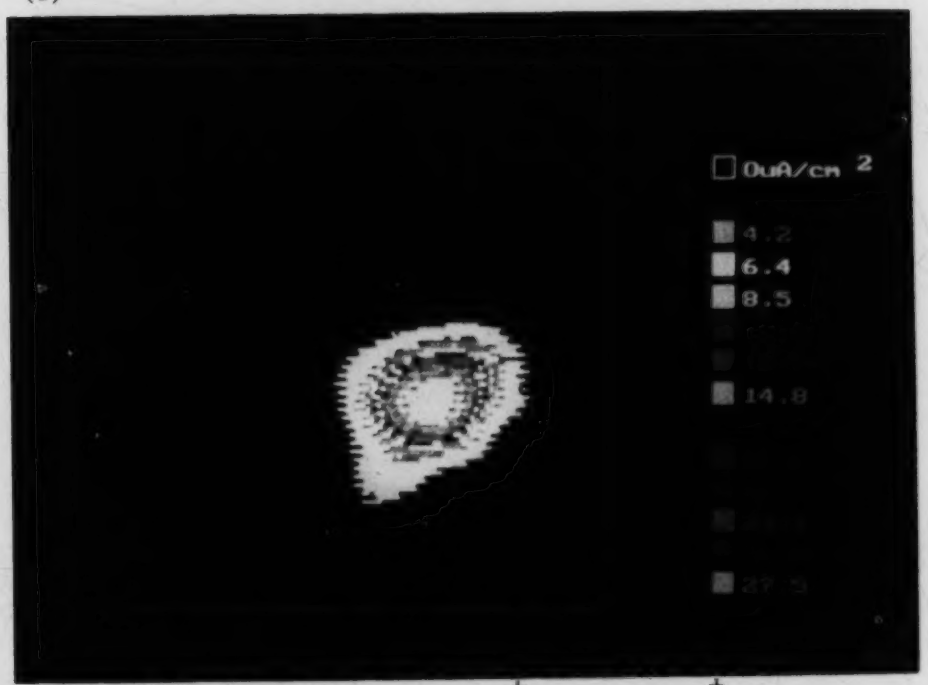

Figure 3.5 Beam profiles of: (a) N_2^+ : and (b) In^+.

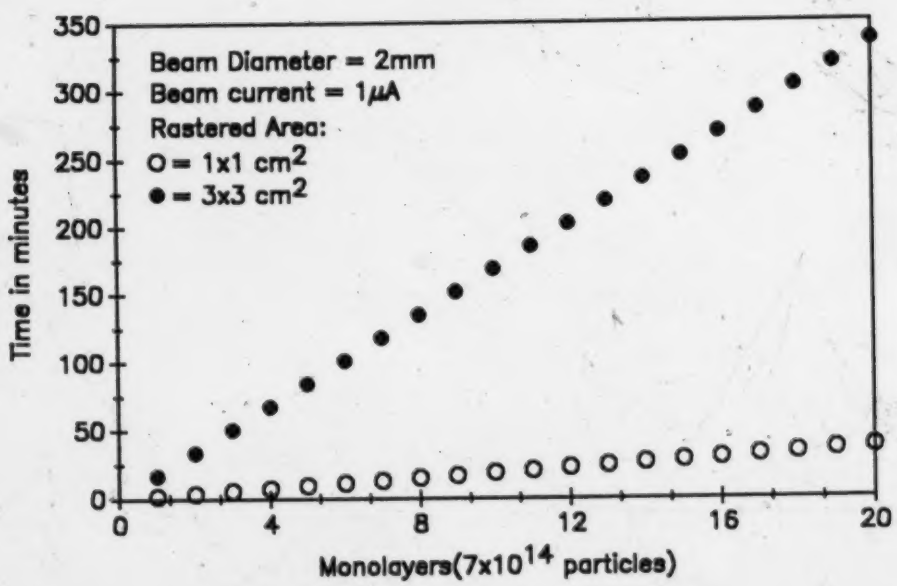

Figure 3.6. Deposition time and thickness (monolayers) as a function of different rastering areas.

Chapter 4. Switching of Sequential Beams

The LEIBS facility constructed at the University of Western Ontario is catered to investigate two processes: (a) the chemical reactions occurring during ion-solid interactions and (b) the growth of new materials. Since the LEIBS houses a single ion source, the growth of new binary compounds and alloys could be difficult. Instead of using two ion sources to supply the film constituents, J. Ahn *et al* has proven that it is possible to grow a binary metastable alloy using a single ion source with two furnaces[1]. One solid material was loaded into each furnace, and the vapor of each material was obtained by filament heating. For example, two different ion species, Pb^+/Mg^+, were generated from such a single ion source in this previous study. By switching the magnetic field of the Wien filter, sequential ion beams of the depositing (ionized) material can be obtained for the growth of binary alloys.

4.1 Ion Source for Sequential Beams

A hot cathode ion source with a single furnace chamber[2], which has been described in chapter 1, was chosen for sequential deposition of indium nitride in the present study. An ion source with a single furnace is used in the present work although J. Ahn *et al*[1] has used an ion source with two furnaces. In the furnace chamber located behind the ionization chamber, a tungsten filament is installed to vaporize the loaded solid material. Then, a carrier gas is passed

through the furnace chamber to flow the resulting gas/vapor mixture into the ionization chamber where the plasma is formed. The resultant ions from the ion source can be a combination of the solid material and the carrier gas if the difference between their ionization potentials is small. Therefore, the single furnace ion chamber is able to provide two ion species from a solid-gas or gas-gas combination.

4.2 Construction

The switching of the magnetic field in the Wien filter is done by an IBM PC computer. The beam switching circuit is incorporated into the high voltage controller since the deflector, Wein filter, and magnetic field power supplies are floating at the beam transport voltage. The computer control of the deflectors and magnetic field is implemented via one Rs232C optical-link. Finally, the output of the D/A (see Fig. 3.4a) is linked to a power supply which supplies current to the magnetic coil inside the Wein filter.

In the preparation of a film growth experiment utilizing two ion species, the computer reads the data from Q1.dat and Q2.dat files which contain the magnet current data pertinent to the masses of two species. To facilitate the growth of a binary compound, magnetic fields are alternated accordingly to perform sequential ion beam switching. The flowchart in Fig. 4.1. shows the decisions made by the computer in alternating the magnetic field of the Wien filter.

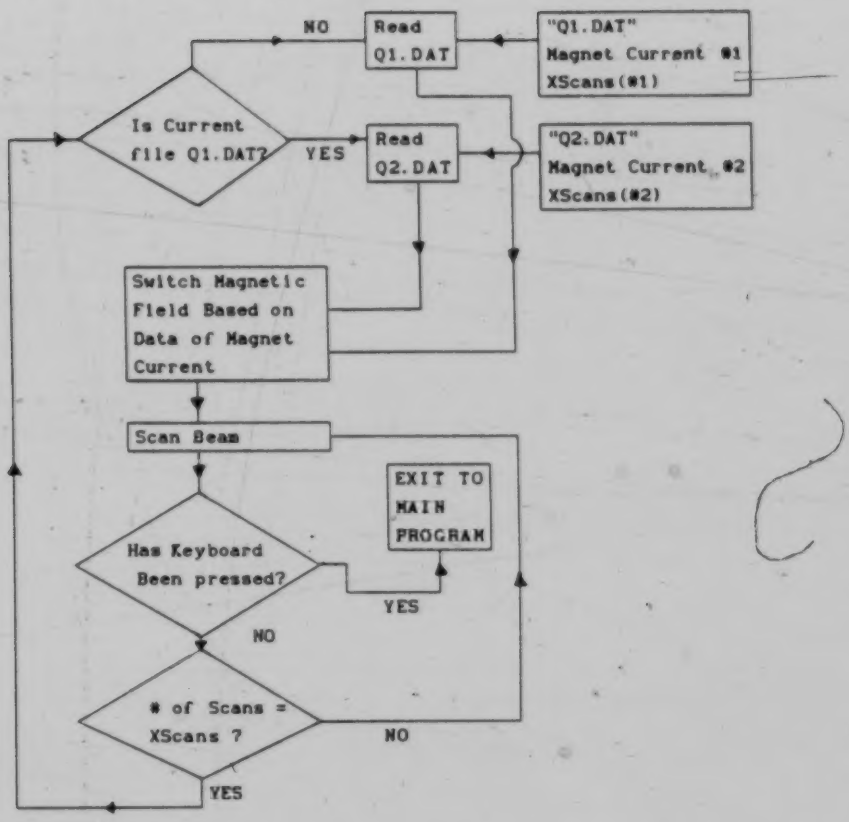

Figure 4.1 Flowchart for the beam switching control.

4.3 Evaluation

The sequential beam switching facility was verified by using the VG quadrupole mass spectrometer. With the QMS operating in the external ion mode (i.e. turning the ionization filament off), the QMS was able to detect the ions entering the target chamber. In the synthesis of indium nitride, In^+ and N_2^+ ions were generated from a single source by placing indium ingots in the furnace chamber of the ion source, and by using pure N_2 as the carrier gas. The N_2 gas pressure was kept at 10 Pa. The current for the furnace filament was kept constant at 8 Amp. It should be noted that indium ions were still detected with the power supply of the furnace filament off. The intense heat from the plasma within the ionization chamber was probably sufficient to provide an adequate vapor pressure of indium (70 Pa at 1200 $^{\circ}C$) although the plasma temperature has not been measured. The anode voltage and the cathode current of the ion source were at 120V and 20A respectively. The impact energies of the ion beams were at 100eV. With the above conditions, the mass spectra of In^+ and N_2^+ during sequential switching are shown in Fig.4.2a and 4.2b. The ion impact energy was verified with the CMA of the QMS and the energy spectrum of the In^+ beam is shown Fig. 4.3.

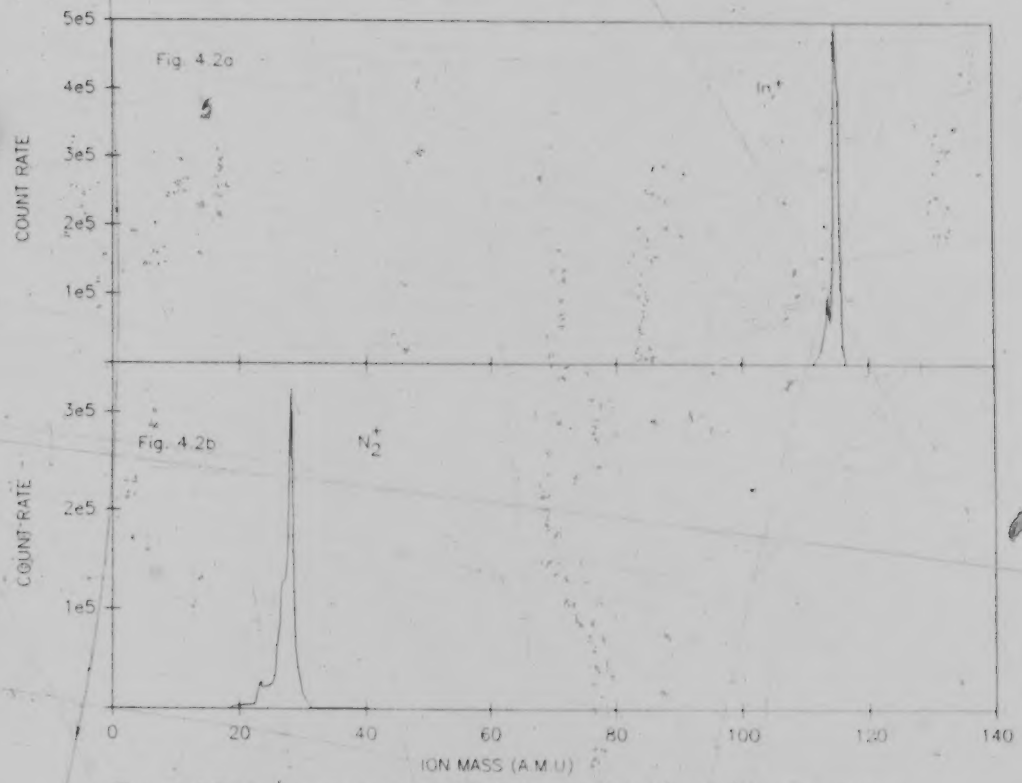

Figure 4.2 Mass spectrum of: (a) In^+; and (b) N_2^+ during sequential ion beams switching.

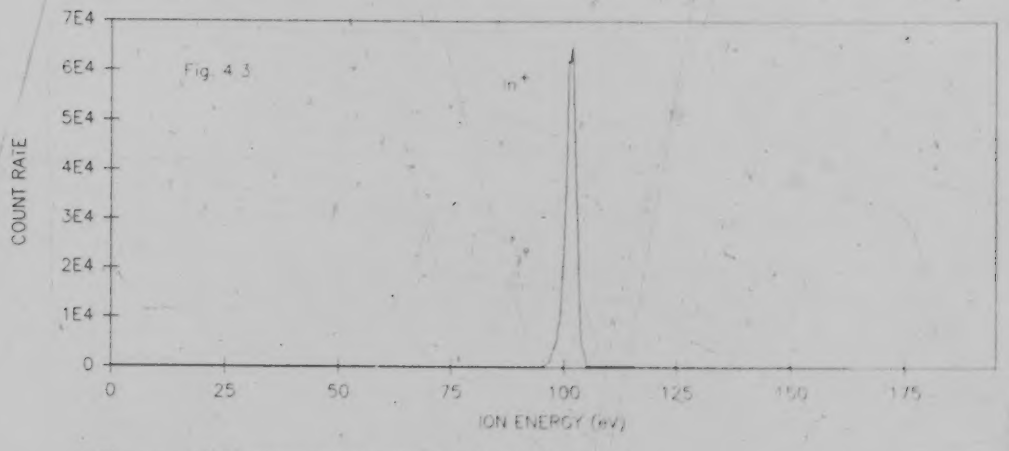

Figure 4.3 Energy spectrum of In^+ at 100 eV.

Part III System Applications

Chapter 5. Thin Film Deposition

5.1 Background

5.1.1 In and InN deposition

Indium Nitride (InN), a III-V semiconductor with a wurtzite crystal structure and a direct band gap (E_g) of about 2.0 eV[1], has become a material of interest in recent years. Because of its relatively high electron mobility[2] (1800 $cm^2V^{-1}s^{-1}$) and direct band gap, it has the potential for high speed electronics and visible light opto-electronics applications. However, to grow InN single crystal is difficult because of the high nitrogen dissociation pressure (> 20 atmospheres at 600°C)[3]. In addition, N_2 is too inert and does not readily combine with indium metal. As such, dissociation of nitrogen molecules is required in the synthesis of InN. So far, InN has been grown successfully by reactive sputtering[4,5], metallorganic vapor phase epitaxy (MOVPE)[6], reactive evaporation[3], ion plating[7], and chemical vapor deposition (CVD)[8].

In the present study, InN was synthesized for the first time, using low energy ion beam deposition with In^+ and N_2^+ bombarding a Si(100) substrate sequentially. In this experiment, the impact energy of the In^+ and N_2^+ ion beams was set at 50eV. The dosage ratio In^+/N_2^+ used in the experiment were about 1:0 and 1:2 which were controlled by computer switching of the magnetic field applied to the Wien filter. The dosage ratio for the special case (1:0) was also included in order to establish a comparison between the metallic In and the

In_xN_y compound for later chemical analysis.

The beam profiles of In^+ and N_2^+ at 50 eV were obtained using the beam profiling method described earlier. It is essential to obtain the beam profiles so as to provide information on dosage calculation and optimum rastering areas. The voltages on the deflectors are -80V and +80V respectively, and the total beam movement is about 10 mm from the beam center (see Eqn 3.3). The maximum current intensities for In^+ and N_2^+ were $28\mu A/cm^2$ respectively. Because of the low current output by the system ($\cong$ 1μA), films of thickness less than 50 Å were growth. Although the vacuum condition during deposition is in the region of 5×10^{-7} Pa, a short deposition time is critical to minimize contamination by residual gases. Since the thickness of the film was less than 50 Å, X-ray photoelectron spectroscopy (XPS), a surface sensitive analytical technique, was used to study the In and InN films.

5.1.2 X-Ray Photoelectron Spectroscopy (XPS)

5.1.2.1 Theory

XPS is a surface sensitive analytical technique which provides both the atomic concentration and chemical bonding states of surfaces. The underlying principle of XPS is the photoelectron effect first proposed by Einstein in 1905[9], which can be observed if a solid in ultra high vacuum (UHV) is irradiated by an X-ray beam. The X-ray beam is usually an Al Kα ($h\upsilon$ = 1486.6 eV) or a Mg Kα ($h\upsilon$ = 1253.6eV) source. The UHV requirement ensures minimum collisions between the

photoelectrons and residual gas molecules. Since the photoelectrons undergo significant inelastic collisions before emerging from the surface, many of these photoelectrons lose significant energy in the collisions within the sample or with the residual gas, and they contribute to the background noise in the total signal. The inelastic mean free paths[10,11] of photoelectrons as a function of kinetic energy in solids are shown in Fig. 5.1. Typical values range from 20 Å to 30 Å from the surface and therefore, XPS is a surface sensitive technique. In XPS, the kinetic energy (K.E.) of a photoelectron ejected from a core level is measured and analyzed. The binding energy (B.E.) of an ejected photoelectron is given by

$$B.E. = h\upsilon - K.E. - \Theta_w \qquad (5.1)$$

where Θ_w is the work function of the analyzer[12]. Since the energy of the incident X-ray beam and the Θ_w of the analyzer are known quantities, the B.E. can be determined easily. A simplified schematic diagram of the photoelectron process[13] is presented in Fig. 5.2.

The B.E. of the electron at core level is defined as the energy difference between the ground state of the electron and the Fermi level[14]. Therefore, element identification is possible because the B.E. of the electron at core level is specific to each element. Furthermore, the B.E. of a core electron is very sensitive to the chemical environment of the atom, and therefore, chemical state for the atom may be determined from the "shifting" of the binding energy[15]. For example, the rearrangement of the valence electrons will change the potential felt by the core electrons. The B.E. of the

core electrons will shift according to the potential change.

5.1.2.2 Instrumentation

The XPS instrument used for the study of the deposited films is a Surface Science Laboratories (SSL) Model SSX-100. A schematic diagram for the XPS setup[16] can be found in Fig. 5.2. The X-ray source is an Al Kα ($h\upsilon$ = 1486.6 eV), and the X-ray beam is produced by bombarding an electron beam on an aluminum anode at 10 kV. X-ray beam monochromatization is achieved with a quartz crystal. Since the X-ray radiation is produced by bombarding an electron beam at the anode, the size of the X-ray spot can be adjusted by focusing or defocusing the electron beam. Typical sizes of the X-ray spots for analysis are: 1) 150 μm; 2) 300 μm; 3) 600 μm; and d) 1000 μm. The Al anode, the crystal and the sample holder are in a Rowland circle configuration[17]. The sample holder is mounted on a vacuum manipulator which enables x, y and z movements to facilitate selected area examination of a sample.

The ejected photoelectrons are collected and focused by an immersion lens. Then, the photoelectrons are retarded to a constant kinetic energy before entering the concentric hemispherical analyzer (CHA) which is most widely used for XPS. The energy of the photoelectrons (pass energy) and the voltage applied on the two sectors also produce a constant absolute analyzer resolution. The energy resolution[18] of the CHA for the SSX-100 XPS is shown in Table 5.1. The CHA is an energy-dispersive device in which photoelectrons

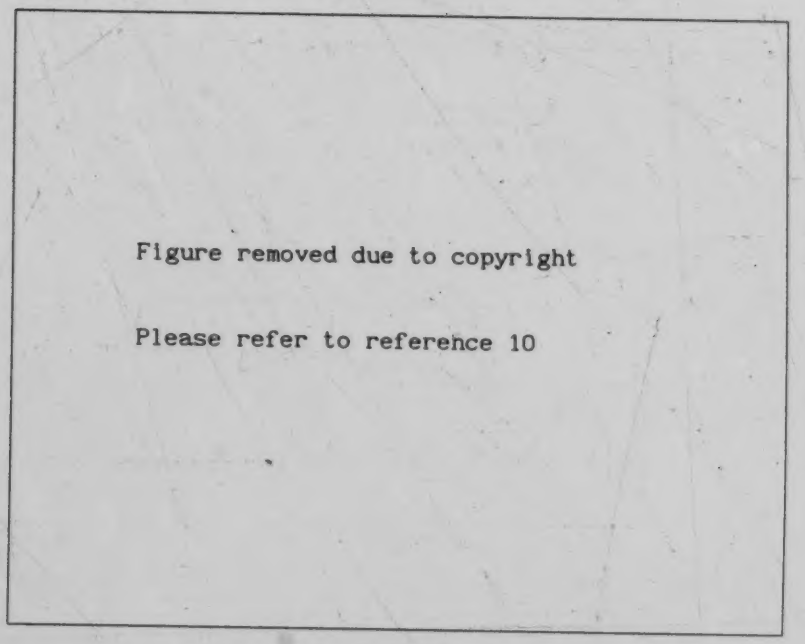

Figure 5.1 Graphical representation of compiled inelastic electron mean free path (IMFP) for elements in monolayers (λ_m) as a function of electron energy.

5.2a

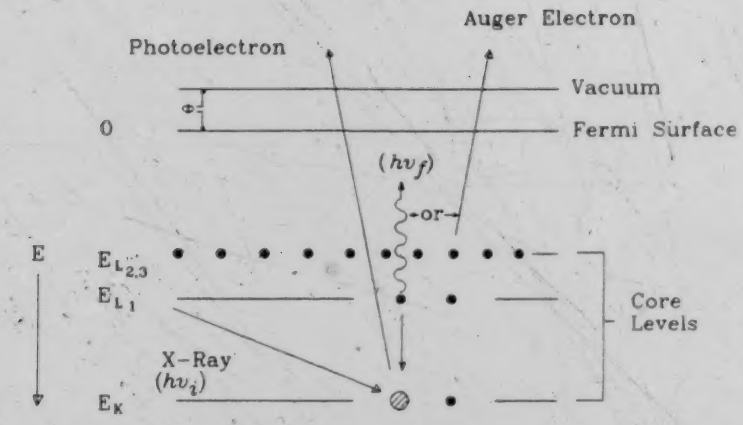

5.2b

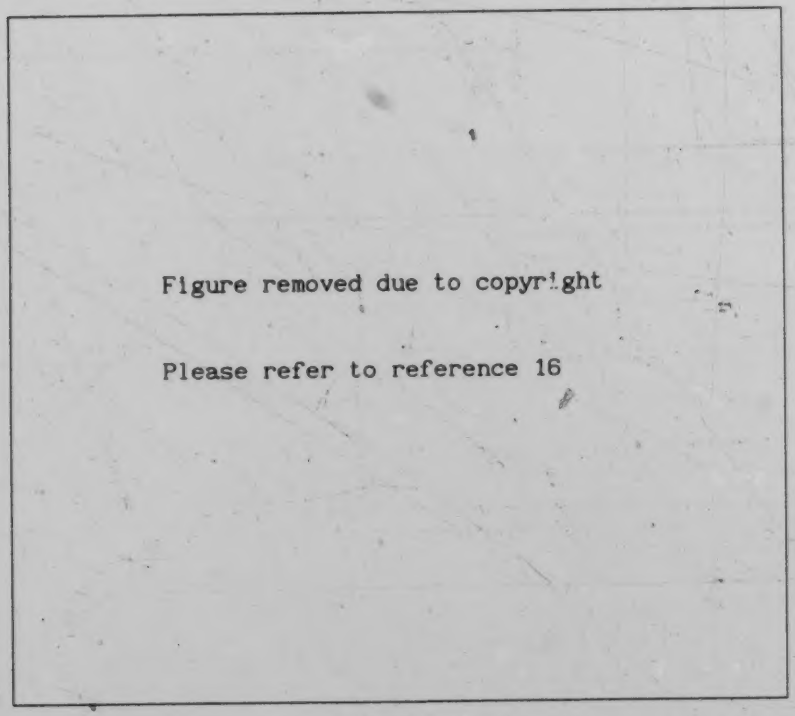

Figure 5.2 (a) Schematic representation of X-ray photoelectron emission process; (b) Instrumentation setup for SSX-100 'small spot' ESCA.

of different energies follow different orbits within the CHA. At resolution 1, i.e. the highest resolution, photoelectrons with 25 eV will pass through the analyzer on the mean circular orbit. Photoelectrons with energy higher than 25 eV will be taking a larger orbit, and the orbit for photoelectrons of lower energy will be smaller.

Resolution	Pass Energy (eV)	Analyzer Resolution (eV)
1	25	0.25
2	50	0.50
3	100	1.00
4	150	1.50

Table 5.1 Relationship between pass energy and analyzer resolution.

A channel plate electron multiplier is placed at the exit of the CHA and serves to amplify the intensity of the photoelectrons. The position-sensitive detector, with resistive anodes, located at the last phase of the detection mechanism decodes the energy spectrum based on the positions where the electrons strike.

The whole XPS instrumental parts are linked by an HP Model 9836 microcomputer. The data or decoded energy spectrum from the position-sensitive detector is collected and stored by the microcomputer. The microcomputer is also equipped with data analysis and manipulation software to perform peak-fitting and surface atomic

composition calculation.

5.2 Results and Discussion

5.2.1 In Films

In the early stage of the experiments, indium thin film was deposited using a stationary beam. The background pressure for the In^+ deposition was about 5×10^{-7} Pa. The impact energy (V_{ip}) of the beam was set at 25 eV. The ion species and energy of the beam were characterized using the VG QMS. The deposited film was analyzed using *in-situ* XPS. The take-off angle with respect to the surface normal for the photoelectrons was fixed at 55°. The background pressure in the XPS was about 5×10^{-7} Pa.

The survey scan for the deposited film is shown in Fig.5.3a. In addition to the indium signals, traces of carbon at 284.3 eV[19] are also recorded in the XPS spectrum. The small amount of carbon is probably surface contamination due to absorption of hydrocarbon. The high resolution In 3d (5/2) spectrum of the film is shown in Fig. 5.3b. The B.E. of the peak was measured to be at 443.9 eV[20,21] which is the typical value for elemental indium. Finally, the valence-band spectra shows that the fermi-level of the deposited In film (Fig. 5.3c) is situated at -0.53 eV. Such a valence band edge position coincided with that of a pure gold standard, which confirms the indium film is metallic. Result from Fig. 5.3b confirms that the degree of purity in the In film deposited by IBD is very high since the B.E. of the deposited film coincided with the B.E. of elemental or pure indium.

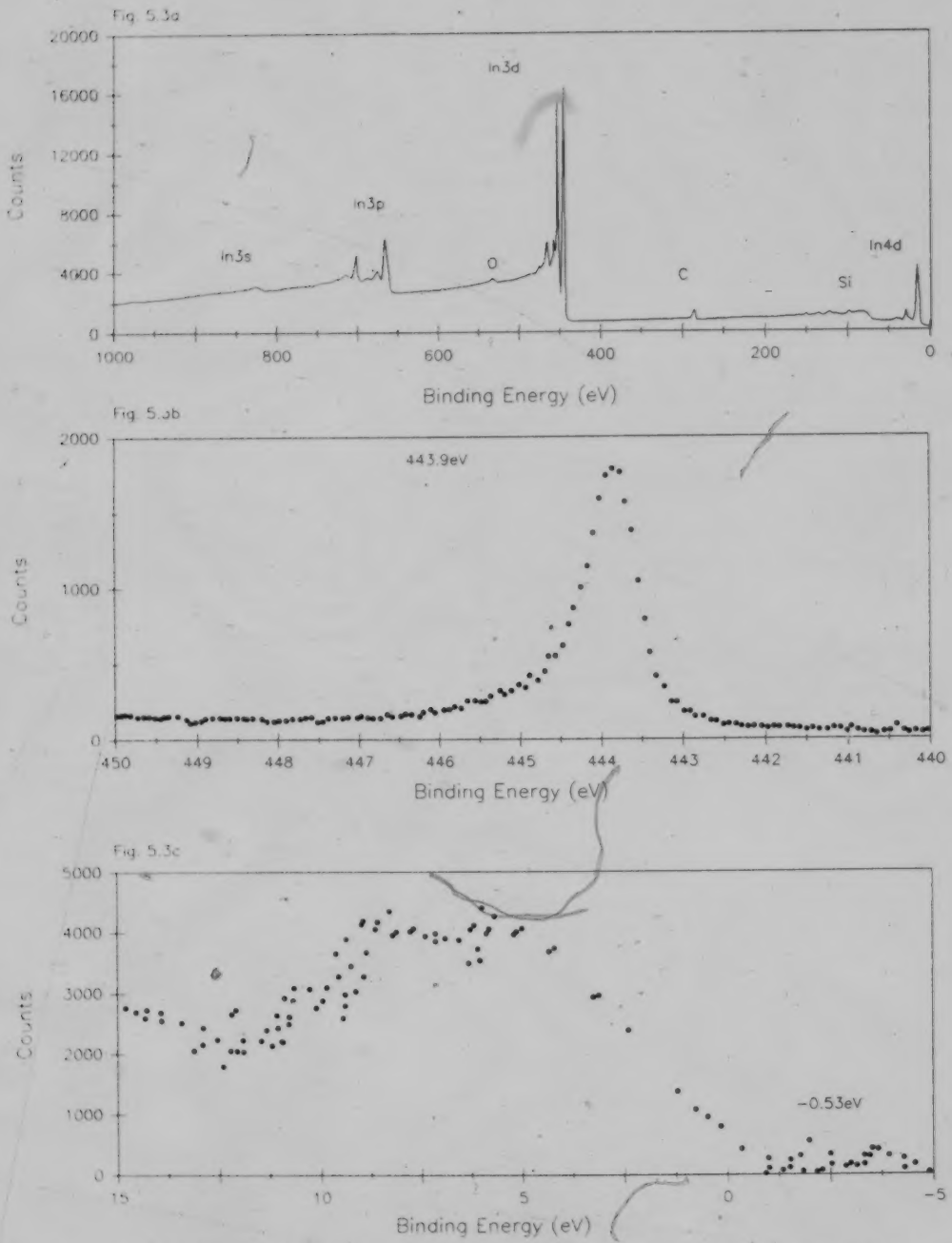

Figure 5.3 XPS spectral outputs of In deposition at different spot sizes and analyzer resolution: (a) survey scan, 300μm, 1.5eV; (b) In window, 300μm, 0.25eV; and (c) valence-band, 300μm, 1.0eV.

Another In film, with V_{ip} = 50 eV was prepared by rastering the beam. The deceleration lens was operating in its five-electrode decelerator-focusing mode to minimize current loss due to space charge effect. About 40% of the total current (1μA) was focused into the 1 mm^2 hole of the Faraday cup. The size and shape of the In^+ beam was digitized using the computerized beam profiling technique described in chapter 3. The profile of the In^+ beam is shown in Fig.3.5b, and the same detailed contour profile is shown in Fig. 5.4. This beam was then rastered over an area of 7 x 7 mm. The thickness of the deposited indium film on Si(100) by rastering the ion beam was determined by XPS. From the intensities of indium and silicon, the thickness of a smooth and homogeneous indium layer on silicon can be determined by[22]

$$t = \lambda \sin(\theta) \ln(I_{In}/I_{Si} + 1) \qquad (5.2)$$

where λ is the inelastic mean free path of the photoelectrons (25 Å) and θ (55°) is the take-off angle of the electron with respect to the surface of the film. The results of the film thickness measured by XPS are plotted in Fig. 5.5. The sudden decrease of indium intensity in Fig. 5.5a is due to blocking by an aperture at the exit of the deceleration lens.

From the size of the beam, a thickness simulation was done using a simple Gaussian function

$$G(k) = \exp\{-[k/(0.63*w)]^2\} \qquad (5.3)$$

where w is the width of the function at FWHM. For a movement of (d*k)

mm from the beam center over a coverage distance of (d*1) mm, the Gaussian function can be modified slightly to give a thickness profile expression

$$J_l = S\sum_k \exp(-[(10-l+k)*d/(0.63*w)]^2) \qquad (5.4)$$

S is a suitable scaling factor and d is the increment step of the Gaussian function. For a movement of 7 mm from the beam center over a coverage distance of 12 mm in the x-direction: l = 0..59; k = 0..34; w = 1.5 mm; and d = 0.2. For rastering in the y-direction, w is 1.9 mm. The simulation results are compared with the real data in Fig. 5.5a and Fig. 5.5b, and both sets of results, in the x and y directions show good agreement.

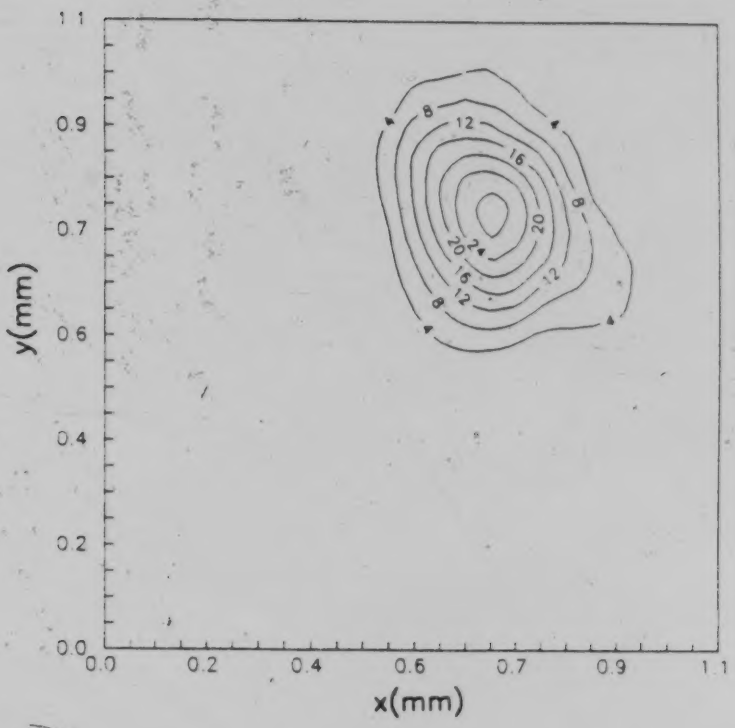

Figure 5.4 In^+ beam profile at 50eV with current contours.

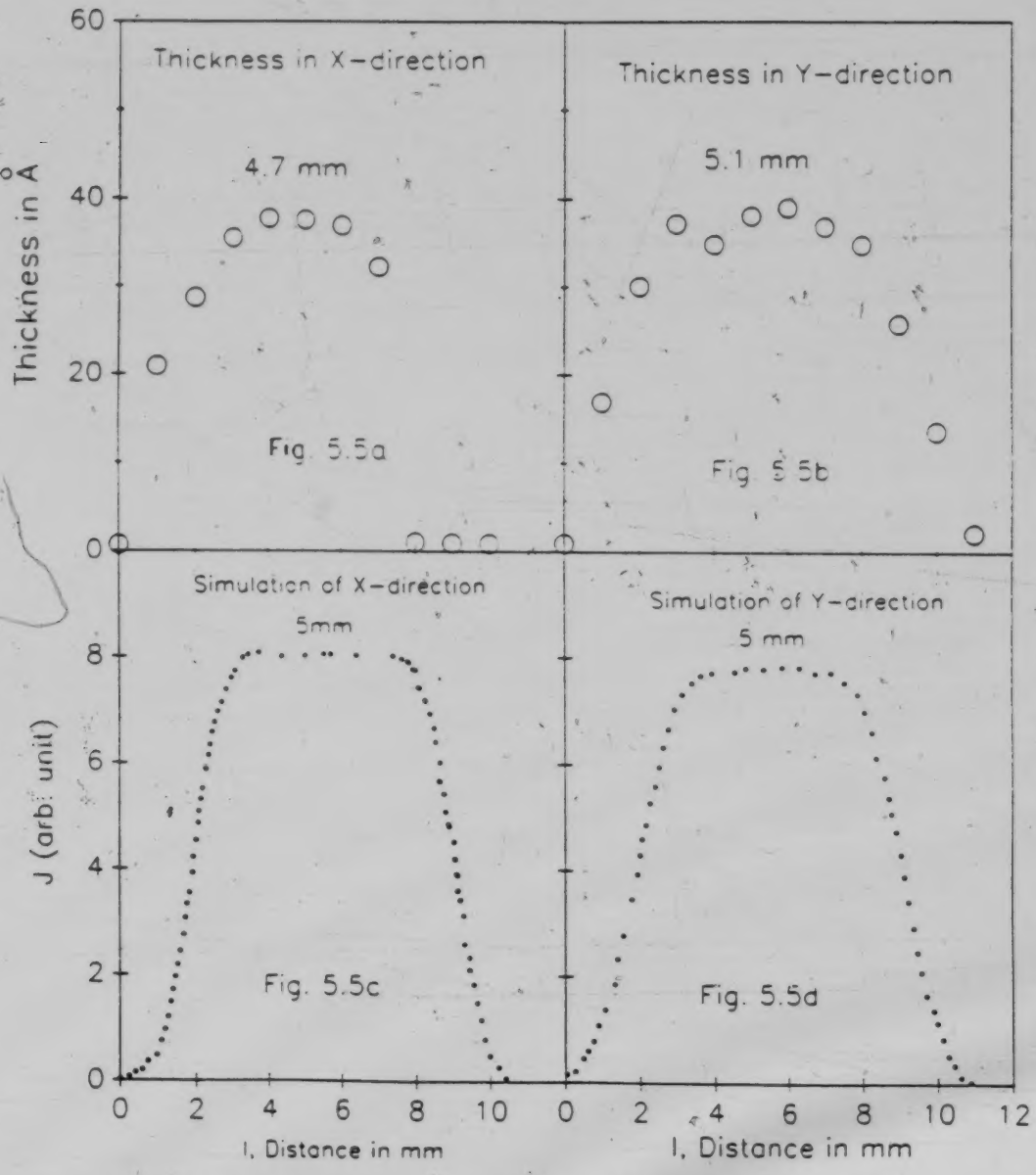

Figure 5.5 Thickness of indium in: (a) x-direction; and (b) y-direction of actual deposition. Thickness of indium in: (c) x-direction; and (d) y-direction from simulation.

5.2.2 Preliminary Results on InN Deposition

In_xN_y was deposited using beam switching, with sequential In^+ and N_2^+ beams incident on a Si (100) substrate. The ion beams, with V_{ip} = 50 eV, were optimized by the deceleration lens operating in a five-electrode mode. The energies and the ion species of the N_2^+ and In^+ beams were characterized by the VG QMS prior to deposition. An In_xN_y thin film of estimated thickness about 50 atom-monolayers was grown. The In/N_2 dosage ratio was about 1:2.

The atomic concentration and the chemical state of the In_xN_y film were studied by XPS. The XPS results for the In_xN_y are shown in Fig.5.6a and 5.6b. In comparison to the pure In film, the inclusion of nitrogen with indium beams shifted the B.E. of indium from 443.9 eV to 444.26 eV. The shifting of B.E. to higher value indicates that the In metal has donated some of the electrons in its valence band to a non-metallic element to form a compound. As a result, the core electrons feel a more "positive" potential, and a larger B.E. is required to eject the negatively charged core electrons in photoemission. The relative valence band edge position was at 0.41 eV which suggests that the In_xN_y film is not metallic. As indicated by the shifting of the valence band edge and the difference in the 3d (5/2) spectrum, it is evident that the addition of N_2^+ bombardment during In^+ dosing converted the metallic In into a non-metallic In_xN_y compound. However, a quantitative XPS data calculation indicated that the In_xN_y ($x \cong 3$, $y \cong 1$) is still very much deficient in N_2 and far

from stoichiometric indium nitride. Therefore, the N_2 incorporation probability is far less than that of In.

XPS analysis of the film-substrate interface showed the presence of silicon at 99.6 eV[23,24] and a silicon compound at 101.5 eV (Fig. 5.7). The peak at 101.5 eV is assigned to silicon nitride which has been reported to have a B.E. at 101.9 eV[23]. Therefore, some of the N_2^+ were consumed by the Si substrate to form silicon nitride. Evidence of film charging was also observed during XPS analysis since silicon nitride is an insulating material. In conclusion, these preliminary results indicate that epitaxial growth of InN on Si substrate will be difficult because of the formation of amorphous silicon nitride[25] at the InN/Si interface.

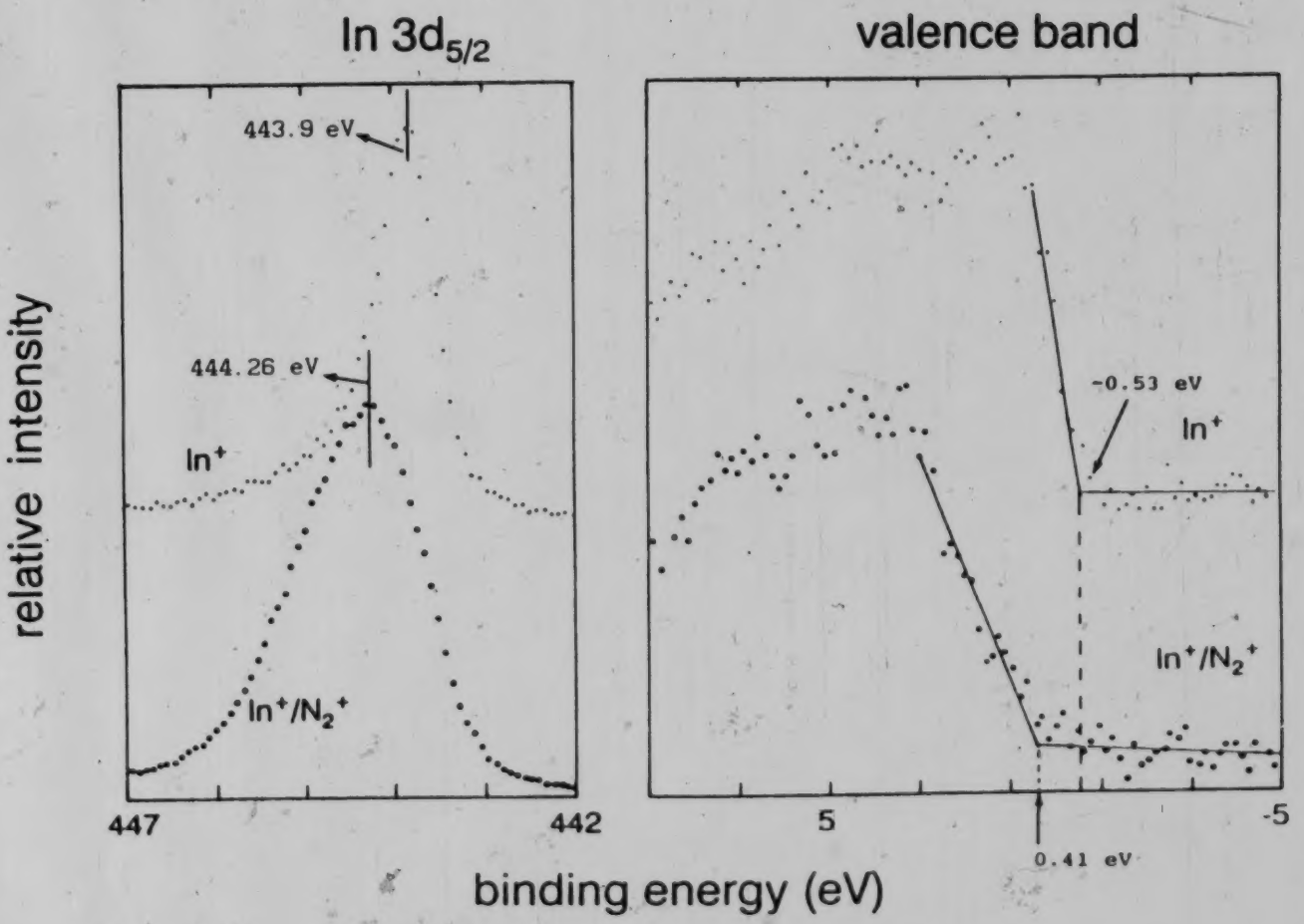

Figure 5.6 XPS spectra of In_xN_y at: (a) In 3d (5/2); (b) valence-band edge.

Formation of silicon nitride at the film-substrate interface

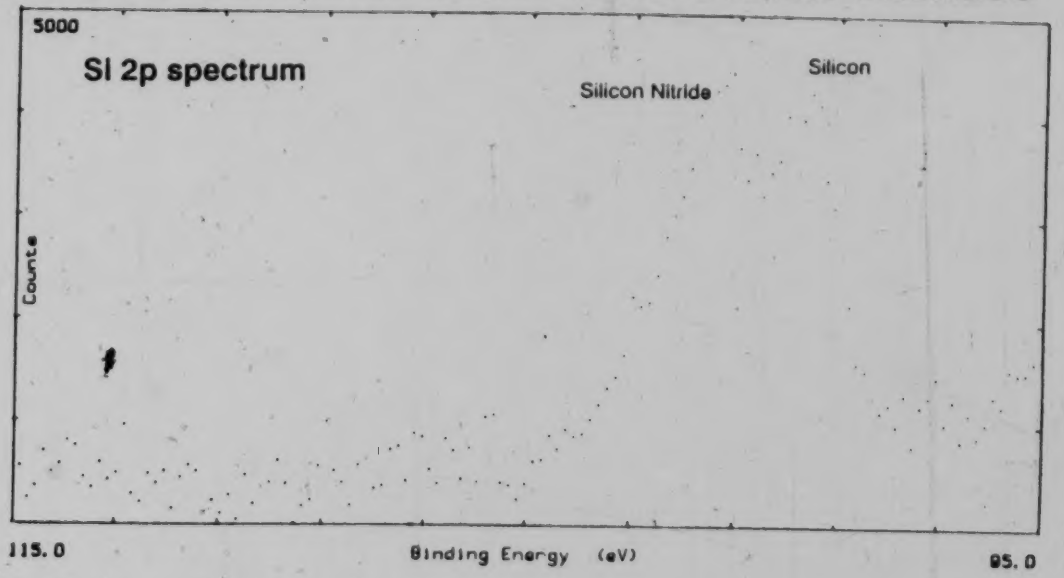

Figure 5.7 XPS spectrum of silicon nitride.

PART IV Conclusions

Chapter 6. Conclusions

The design, construction and evaluation of a five-electrode deceleration lens for low energy ion transport have been performed. From the simulation and experimental results, the design of this five-electrode deceleration has been shown to alleviate beam spreading due to the space-charge effect. Our results indicate that the present five-electrode lens is a flexible ion deceleration system suitable for delivering ion beams to a grounded target with a current density higher than 10 $\mu A/cm^2$ at impact energy of 10eV. Experiments with Ar^+, In^+ and N_2^+ ion beams have shown that the beam handling systems behave well between energies of 10 eV - 200 eV.

A thin film of indium was deposited using the beam rastering/scanning unit. Results from XPS have confirmed the uniformity and the high purity of the indium film deposited by LEIBD. The beam mass-switching facility has been characterized by a QMS. Separate mass spectra of In^+ and N_2^+ beams were obtained during the mass-switching operation.

The beam profiling monitor, rastering and switching facilities have proven their usefulness in the deposition of In_xN_y. When a dose ratio (In/N) of 1:2 was used, In_3N_1 was formed indicating that the sticking coefficient of nitrogen is less than that of indium.

Part V References

References (Chapter 1)

[1] L.G. Meiners, Ru-Pin Pau and J.R. Sites, J. Vac. Sci. Technol. 4(1977) 961.

[2] W.D. Westwood and S.J. Ingrey, J. Vac. Sci. Technol. 13(1976) 104.

[3] A.E.T. Kuiper, G.E. Thomas and W.J. Schouten, J. Crystal Growth 51(1981) 17.

[4] T. Takagi, I. Yamada and Sasaki, Thin Solid Films 45 (1975) 569.

[5] J. Ahn, R.P.W. Lawson, K.M. Yoo, K.A. Stromsmoe and M.J. Brett, Nucl. Instr. and Meth. B17(1986) 34.

[6] N. Herbots, O.C. Hellman, P.A. Cullen and O. Vancauwenberghe, in *Semiconductor-Based Heterostructure Formation Using Low Energy Ion Beams: Ion Beam Deposition (IBD) & Combined Ion Molecular Beam Deposition (CIMD)*, Ed. G.W. Rubloff, Amer. Vac. Soc. Ser., 4(1988) 259.

[7] T.E. Haynes, R.A. Zuhr, S.J. Pennycook and B.R. Appleton, Appl. Phys. Lett., 54(1989) 1439.

[8] N. Herbots, B.R. Appleton, T.S. Noggle, R.A. Zuhr and S.J. Pennycook, Nucl. Instr. and Meth. B13(1986) 250.

[9] D.G. Armour, P. Bailey and G. Sharples, Vacuum 36(1986) 769.

[10] J. Amano, Thin Solid Films 92(1982) 115.

[11] S. Shimizu, O. Tsukakoshi, S. Komiya and Y. Makita, Jpn. J. Appl. Phys. 24(1985) 1130.

[12] P.C. Zalm and L.J. Beckers, Appl. Phys. Lett., 41(1982) 167.

[13] G.E. Thomas, L.J. Beckers, J.J. Vrakking and B.R. DE Koning, J. Crystal Growth 56(1982) 557.

[14] K. Miyake and T. Tokuyama, Thin Solid Films, 92(1982) 123.

[15] R.A. Zuhr, S.J. Pennycook, T.S. Noggle, N. Herbots, T.E. Haynes and B.R. Appleton, Nucl. Instr. and Meth. B37/38(1989) 22.

[16] J. Ahn, K.A. Stromsoe and R.P.W. Lawson, IEEE Trans Indust. Elect. IE-32(1985) 405.

[17] T. Tsukizoe, T. Nakai and N. Ohmae, J. Appl. Phys. 48(1977) 4770.

[18] I. Yamada, H. Inokawa and T. Takagi, Nucl. Instr. Meth. B6(1985) 439.

[19] I. Yamada, 7th Int. Conf. on Ion Beam Modification of Materials, Knoxville, Tennessee, USA (1990).

[20] Documentation [1] distributed by Colutron Research Corp., 2321 Yarmouth Ave., Boulder, CO 80301, USA.

[21] J.H. Freeman and G. Sidenius, Second Int. Conf. Ion Sources, Wien(1972) 724.

[22] R.G. Wilson and G.R. Brewer, *Ion Beams*, John Wiley & Sons Inc., New York (1973).

[23] I. Langmuir, Phys. Rev., 2(1913) 450.

[24] Documentation [2] distributed by Colutron Research Corp., 2321 Yarmouth Ave., Boulder, CO 80301, USA.

[25] J. Amano and R.P.W. Lawson, J. Vac. Sci. Techno. 15(1978) 118.

[26] H. Ryssel and I. Ruge, *Ion Implantation*, John Wiley & Sons, Chichester (1986).

[27] A. Berman, *Total Pressure Measurements in Vacuum Technology*, Academic Press, Orlando (1985).

[28] P.H. Dawson and N.R. Whetten, Dyn. Mass Spectrom., 2(1969) 1.

[29] D. Briggs and M.P. Seah, *Practical Surface Analysis by Auger and X-ray Photoelectron Spectroscopy*, John Wiley & Sons, Chichester (1983).

[30] N.W. McLachlan, *Theory and Application of Mathieu Functions*, Oxford University Press, Oxford (1951).

References (Chapter 2)

[1] Gy.A. Nagy and M. Szilagyi, *Introduction to the theory of space charge optics*, 2nd ed., Halsted Press, New York, 1974.

[2] D. G. Armour, P. Bailey and G. Sharples, Vacuum 36, 11/12(1986) 769.

[3] Z. Herman, J.D. Kerstetter, T.L. Rose, and R. Wolfgang, Rev. Sci. Instrum. 40(1969) 538.

[4] H. Liebl, J. Bohdansky, J. Roth and V. Dose, Rev. Sci. Instrum. 58(1987) 1830.

[5] CHDEN, Focussed Software, 871 Southgate Drive, State College, PA 16801, USA.

[6] G.P. Malafsky and N. Winograd, Rev. Sci. Instrum. 59(1988) 1294.

[7] M. Szilagyi, *Electron and Ion Optics*, Plenum Press, New York (1988).

[8] M. Abramowitz and I.A. Stegun (eds), *Handbook of Mathematical Functions*, Dover, New York (1972).

References (Chapter 3)

[1] S. Shimizu, O. Tsukakoshi, S. Komiya, and Y. Makita, Jpn. J. Appl. Phys., 9(1985) 1130.

[2] J. Ahn, R.P.W. Lawson, K.M. Yoo, K.A. Stromsmoe, and M.J. Brett, Nucl. Instr. and Meth., B17(1986)37.

[3] G.E. Thomas, L.J. Beckers, J.J. Vrakking, and B.R. De Koning, J. Crystal Growth, 56(1982)557.

[4] Motorola CMOS Integrated Circuits, Motorola, 1978.

[5] Data Conversion Products Databook, Analog Devices, 1988.

References (Chapter 4)

[1] J. Ahn, R.P.W. Lawson, K.M. Yoo, K.A. Stromsoe and M.J. Brett, Nucl. Instr. and Meth. B17(1986) 37.

[2] J. Amano and R.P.W. Lawson, J. Vac. Sci. Techno., 15(1978) 118.

References (Chapter 5)

[1] T.L. Tansley and C.P. Foley, J. Appl. Phys., 59(1986) 3241.

[2] T.L. Tansley and C.P. Foley, Electron. Lett., 20(1984) 1066.

[3] Y. Sato and S. Sato, Jpn. J. Appl. Phys., 28(1989) 1641.

[4] H.J. Hovel and J.J. Cuomo, Appl. Phys. Lett., 20(1972) 71.

[5] K. Westra, M. Sc. Thesis, University of Alberta, 1989.

[6] A. Wakahara and A. Yoshida, Appl. Phys. Lett., 54(1989) 709.

[7] O. Takai, J. Ebisawa and Y. Hisamatsu, Proc. 7th Int. Conf. Vac. Metall., Tokyo, 1982(1982) 137.

[8] O. Takai, J. Ebisawa and Y. Hisamatsu, Proc. 7th Int. Conf. Vac. Metall., Tokyo, 1982(1982) 129[9] A. Einstein, Ann. Phys., 17(1905) 132.

[10] M.P. Seah and W.A. Dench, Surf. Interface Anal., 1(1979) 1.

[11] S. Tanuma, C.J. Powell and D.R. Penn, Surf. Interface Anal., 11(1988) 577.

[12] L.C. Feldman and J.W. Mayer, *Fundamentals of Surface and Thin Film Analysis*, North-Holland, New York (1986).

[13] EE642 Course Materials.

[14] K. Siegbahn, C.N. Nordling, A. Fahlman, R. Nordberg, K. Hamrin, J. Hedman, G. Johansson, T. Bermark, S.E. Karlsson, I. Lindgren, B. Lindberg, *ESCA: Atomic, Molecular and Solid State Structure Studied by Means of Electron Spectroscopy*, Almqvist and Wiksells, Uppsala (1967).

[15] K. Siegbahn, Nordling, E. Sokolowski, *in Proc. Rehovoth Conf. on Nuclear Structure*, Ed. H.J. Lipkin, North-Holland, Amsterdam (1958) 291.

[16] C.D. Wagner and A. Joshi, Surf. Interface Anal. 6(1984) 215.

[17] R.L. Chaney, Surf. Interface Anal. 10(1987) 36.

[18] Personal communication with Dr. W.M. Lau.

[19] T.A. Carlson, *Photoelectron and Auger Spectroscopy*, Plenum Press, New York (1975).

[20] C.D. Wagner, W.M. Riggs, L.E. Davis, J.F. Moulder and G.E. Mullenberg, *Handbook of X-Ray Photoelectron Spectroscopy*, Perkin-Elmer Corporation, Physical Electronics Division, Eden Prairie, Minnesota (1979).

[21] D. Briggs and M.P. Seah, *Practical Surface Analysis by Auger and X-ray Photoelectron Spectroscopy*, John Wiley & Sons, Chichester (1983).

[22] B.R. Strohmeier, Surf. Interface Anal. 15(1990) 51.

[23] J.E. Castle and R.H. West, J. Electron Spectrosc., 18(1980) 355.

[24] J.A. Taylor, Appl. Surf. Sci., 7(1981) 168.

Part VI VITA

VITA

Name : Kok-Ken Foo
Place of Birth : Seria, Brunei
Year : 1964

Academic Background

(1989-1990) **University of Alberta**
Candidate for M.Sc. in Electrical Engineering.

(1986) **University of Alaska-Fairbanks, Alaska, USA**
Bachelor of Science in Electrical Engineering.

Working Experience

(1989-90) **University of Alberta/Western Ontario**
Graduate assistant and Teaching assistant.

(1987-89) **Cemtronix Pte. Ltd., Kuala Lumpur, Malaysia.**
System engineer for Building Automation Designs.

(1984-86) **University of Alaska**
Teaching Assistant for E.E. Dept. and system analyst for Geophysical Institute.

Publications

Deceleration and Ion Beam Optics in the regime of 0 - 200 eV.
K.K. Foo, R.P.W. Lawson, W.M. Lau and X. Feng
(submitted to JVST on Aug, 90).

A Combined Beam Profiling and Rastering Technique.
K.K. Foo and R.P.W. Lawson
(submitted to JVST on Sept, 90).

Construction, Characterization, and Applications of a mass-resolved Low Energy Ion Beam System.
W.M. Lau, X. Feng, S. Sant, I. Bello, K. Foo and R.P.W. Lawson
(presented at 7th Int. Conf. on IBMM 90).